UNIVERSITY OF CALIFORNIA
SANTA CRUZ

MECHANISTIC INSIGHTS INTO LIGHT-GATED ANION CHANNELS FROM *GUILLARDIA THETA*

A dissertation submitted in partial satisfaction
of the requirements for the degree of

DOCTOR OF PHILOSOPHY

in

CHEMISTRY

by

Pamela Schleissner

September 2022

The Dissertation of Pamela Schleissner is approved:

_____
Professor David Kliger, Chair

_____
Professor Ólöf Einarsdóttir

_____
Professor Carrie Partch

_____
Peter Biehl
Vice Provost and Dean of Graduate Studies

Table of Contents

List of Figures

List of Tables

Abbreviations

ACR	anion channelrhodopsin
ATR	all-*trans* retinal
BMGY	buffered glycerol-complex medium
BMMY	buffered methanol-complex medium
BR	bacteriorhodopsin
ChR2	cation channelrhodopsin from *Chlamydomonas reinhardtii*
DDM	n-dodecyl-β-D-maltoside
EDTA	ethylenediaminetetraacetic acid
G. theta	*Guillardia theta*
GtACR	anion channelrhodopsin 1 from *Guillardia theta*
HCl	hydrochloric acid
HEPES	4-(2-hydroxyethyl)-1-piperazineethanesulfonic acid
IPTG	isopropyl β-d-1-thiogalactopyranoside
LB	lysogeny broth media
NaCl	sodium chloride
NaOH	sodium hydroxide
MWCO	molecular weight cut off
PMSF	phenylmethylsulfonyl fluoride
SVD	singular value decomposition
TROD	time-resolved optical density used for time-resolved absorption spectroscopy
WT	wild-type
YPD	yeast extract-peptone-dextrose

Abstract

Mechanistic Insights into Light-Gated Anion Channels from *Guillardia theta*

Pamela Schleissner

The most effective optogenetic tools available for neuronal silencing are the light-gated anion channels found in the cryptophyte alga *Guillardia theta* (*Gt*ACRs). *Gt*ACRs have the highest chloride-conductance among natural or synthetic anion-conducting channelrhodopsins. Molecular mechanisms of *Gt*ACRs are of great interest for understanding this exceptional conductance. The ion transport of GtACRs are intimately tied to their photochemical reaction mechanism in which the lifetimes of open channel photointermediates regulate the channel conductance. So far, no studies have been able to accurately pinpoint the photointermediate corresponding to the open channel state. In this thesis, the photoreactions of wild-type GtACR1 and variants are investigated through multichannel time-resolved absorption spectroscopy. The results presented here demonstrate the existence of isospectral photointermediates and identify a previously unknown photointermediate. Additional insights into the photomechanism are made and a new open channel photointermediate is proposed. This contribution to unraveling channelrhodopsin mechanisms will help elucidate the underpinnings of GtACRs unusually high conductance and facilitate improved rational design of molecular tools for optogenetic applications.

This thesis is dedicated to my grandmother.
If resiliency is an inherited trait,
then I know my resiliency comes from you.

Acknowledgements

I want to acknowledge the teachers and mentors who contributed to my understanding and helped me achieve this significant work of my formal education. I would first like to thank my advisor, Professor Dave Kliger, whose patience, wisdom, guidance, and encouragement were instrumental in the success of this project. I want to thank the chair of my committee, Professor Ólöf Einarsdóttir, for her astute advice and for the use of her laser system. I would also like to thank my committee member, Professor Carrie Partch. I am deeply grateful for the inclusion in your lab to learn molecular biology and for your honest, insightful advice.

This work was made possible through the generous help of Istvan Szundi. I appreciate all you've done for this project, and I'll miss your Hungarian jokes. I want to acknowledge Eefei Chen for her helpful advice on experimental techniques and for maintaining a sense of community within the lab. And to the other members of the Kliger Research Group: Bob, Ray, Stephanie, and Addis, thank you all for the interesting discussions.

The members of the Partch Research Group were of vital support and guidance with the techniques required to express and purify the materials used in this work. Thank you for including me as an honorary member of your lab. I want to acknowledge Professor Doug Kellogg, Professor Seth Rubin, Professor Ted Holman, Professor John MacMillan, and all the members of their research groups for allowing me to use their facilities and providing helpful advice.

I want to acknowledge Professor John Spudich (The University of Texas Health Science Center at Houston) and the members of his lab group, particularly Dr. Hai Li and Dr. Yumei Wang. Thank you for troubleshooting purification techniques with me and for providing the mutant strains used in this work.

I want to thank my students who elicited revisiting topics in chemistry, sometimes gaining new perspectives, and always reminding me why I enjoy this subject so much. I want to thank my friends, partners, and siblings, who were all vital sources of peer mentorship and support outside the lab. Finally, I want to acknowledge my parents, my first teachers in life. My deepest love and gratitude for all that you've taught me, and for guiding me onto this fulfilling life path.

Ars longa, vita brevis.

-Hippocrates

Learning is a weightless treasure you can always carry easily.

-Chinese proverb

CHAPTER 1

General Introduction

Life on earth evolved with the influence of sunlight, and nearly all living organisms have some variation of light reception. Specialized molecules called photoreceptors are responsible for sensing light in the environment and converting the signal into a series of chemical events. Various biological processes depend on photoreceptors, including circadian rhythms, gene regulation, visual perception, photosynthesis, photomotility, phototropism, and photomorphogenesis. Of the molecules responsible for light reception, rhodopsins are among the oldest on earth and found in all domains, Eukaryotes, Prokaryotes, and Archaea.[1]

Rhodopsins are retinylidene proteins that share a seven trans-membrane alpha helix domain (opsin) with a retinal cofactor (chromophore). Their functional process starts with the photoisomerization of a retinal cofactor that triggers conformational changes of the opsin backbone, which, in turn, initiates downstream chemical events. Rhodopsins are categorized into two types. Although the two types share a similar structure, an opsin scaffold with a covalently linked retinal through a Schiff base on the seventh helix, they have no sequence homology. The mechanisms between the two types are also different. Microbial rhodopsins (Type I) have a retinal chromophore that starts in an all-trans configuration and photoisomerizes into a 13-cis configuration. Type II, the metazoan rhodopsins, are most prevalent in the visual processes of animals and have a retinal chromophore that converts from the 11-cis to an all-trans configuration upon absorption of light. Other photoisomerization variations also exist in nature; for a review see ref. [2] Of the two types, Type I has a much greater functional diversity.

1.1 Functional Diversity of Microbial Rhodopsins

First discovered in the 1970s, bacteriorhodopsin (BR) from *Halobacterium salinarum* serves as the archetypal Type I microbial rhodopsin. BR is the primary receptor responsible for producing energy in the microbe through photosynthesis. It works by shuttling protons, one proton per cycle, across the outer membrane, creating an electrochemical gradient that is subsequently converted into chemical energy. Since the discovery of BR, various microbial rhodopsins have been discovered and shown to serve other functions, including regulating cell processes through signal transduction pathways. The microbial rhodopsins that function as sensory receptors are split into two categories. The first relays sensory information through enzymatically active subunits or secondary proteins. These include the sensory and histidine kinase rhodopsins. The second category consists of the channelrhodopsins, which function as light-gated passive ion channels, funneling hundreds of ions per cycle, that directly relay sensory information through a change in the electrochemical gradient across the cell membrane.[2] The following sections describe channelrhodopsins in more detail with particular emphasis on the variants used in this study.

1.2 Channelrhodopsins

Channelrhodopsins have received a considerable amount of attention in the last decade as they provide a means to control functions of neurons with light using a technique called optogenetics. Optogenetic experiments are carried out by expressing channelrhodopsins in a population of neurons under the control of cell-specific promoters. The cells that express the protein are then photoactive, and light stimulation

results in activation or suppression via hyperpolarization or depolarization, respectively. The technique has broadened the understanding of the involvement of groups of neurons in complex processes, including decision making, learning, memory, epilepsy, and chronic pain.[3–8] Clinical applications are currently being investigated. Recently, a Phase III clinical trial successfully restored partial vision in a blind human using optogenetics.[9]

The first channelrhodopsin to be successfully used in optogenetics was the cation channelrhodopsin 2 (ChR2) from *Chlamydomonas reinhardtii*.[2] ChR2 primarily conducts protons but is capable of conducting other cations, including Na^{2+}, Mg^{2+}, and guanidinium^{+}. When expressed in neurons, ChR2 increases activity by depolarizing the membrane. Since the discovery of ChR2, the number of channelrhodopsins has steadily increased. In 2012, the genome of the first representative cryptophyte alga, *Guillardia theta* (*G. theta*), was reported.[10] Through a BLAST of the cryptophyte alga's genome, two anion channelrhodopsins (ACRs) were discovered in 2015.[11] The passive anion flow in ACRs provides a means to hyperpolarize the membrane and suppress neuronal activity. The ACRs from *G. theta* have been shown to inhibit activity and control behavior in a wide-range of living animals, and show promise in a number of research applications.[12–15] Of the two anion channelrhodopsins from *G. theta*, only GtACR1 is known to maintain its ion conductance *in vitro.*[16] The following sections will describe what is known about the structure and mechanism of GtACR1.

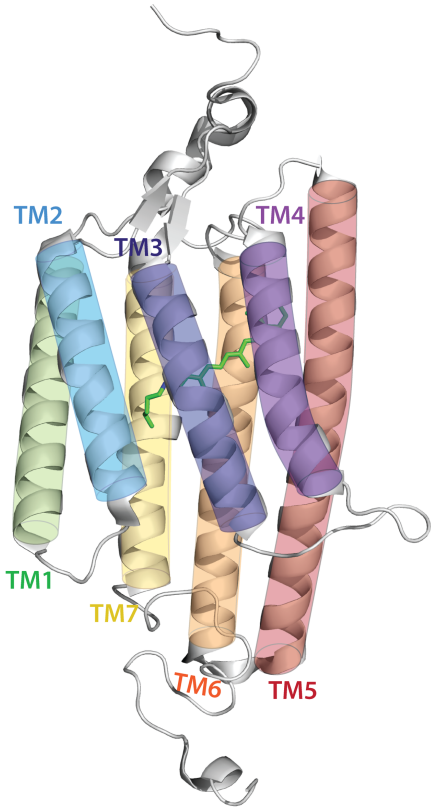

Figure 1.3.1: Structure of GtACR1 with color coded transmembrane helices. All-trans retinal is colored in green. PDB: 6EDQ

1.3 Structure of the Anion Channelrhodopsin

GtACR1 and ChR2 have a low sequence homology (~24%) but a high structural homology (R.M.S.D. 0.9 Å).[16] Akin to all microbial rhodopsins, GtACR1 and ChR2 both contain a 7 trans-membrane alpha helix domain and a retinal covalently attached through a protonated Schiff base linkage on the seventh helix. Confocal near-infrared resonance Raman found the retinal in GtACR1 to exist in the all-*trans* configuration and time-resolved Fourier transform infrared spectroscopy experiments revealed GtACR1 does not enter a light-adapted state, validating the all-*trans* configuration in

the unphotolyzed state.[17,18] This differs from ChR2, which has been found to adopt either an all-*trans* C_{15}=N-*anti* or a 13-*cis* C_{15}=N-*syn* configuration in the unphotolyzed state.[19] The channel of GtACR1 forms between transmembrane helices 1,2,3, and 7, and was found to be lined with polar and aliphatic residues. The extracellular side was abundant in electropositive residues, allowing the protein to selectively permit anions across the membrane.[16,20] The retinal Schiff base intersects the channel near the tightest constriction site but does not directly form the constriction. Instead the constriction site is formed by the neighboring T101, L64, and M105 residues.[16] It was hypothesized that certain charged residues in the channel of ChR2 are responsible for imparting cation conduction. One of these residues, E97, corresponds to A75 in GtACR1, a conserved non-carboxylate in anion channelrhodopsins. When mutated to a glutamate, A75E did not change the ion selectivity, but instead reversed the direction of rectification.[16,21] A75E also had significantly less photocurrent and a slower decay.[21,22]

There is an open question of how the Schiff base is neutralized in GtACR1. In BR, neutralization of the protonated Schiff base involves a water molecule, D212 (D234 in GtACR1), and D85 (S97 in GtACR1).[2,23] In all anion channelrhodopsins, a conserved non-carboxylate group is in the D85 position (S97) and cannot serve as a proton acceptor. Moreover, mutation of serine to glutamate (S97E) resulted in reduced photocurrents, which highlighted the functional importance of a non-carboxylate group at this position.[24] There has been no evidence of water or chloride ions near the protonated Schiff base in GtACR1. Only D234 is weakly interacting and presumably this residue is responsible for neutralization in the unphotolyzed state. However, the

jury is still out on whether the D234 residue is protonated. Resonance Raman and X-ray crystallography experiments found the residue to be protonated and neutralization of the Schiff base originating from nearby tyrosine residues, Y72 and Y207, interacting with D234 to produce a partial negative charge on the residue.[16,18,20] However, room temperature FTIR and MD simulations found D234 to be deprotonated, with Y72 and Y207 capable of interacting with only the deprotonated form of the D234 residue.[17,25] Electrophysiology results from the D234N mutant reported significantly diminished photocurrents implying a loss-of-function.[20] This observation is explained easily if the D234 residue is deprotonated. The mixed results from different experimental techniques warrant further investigations.

1.4 Kinetics and Mechanism of the Anion Channelrhodopsin

The channel kinetics of GtACR1 can be monitored *in vivo* through whole-cell patch clamp electrophysiology. Electrophysiology experiments under single turnover conditions, where no secondary photoexcitation occurs, revealed two distinct channel mechanisms, one involving a fast rise and slow decay, and the other a slow rise and fast decay.[26] The fast and slow rise times were reported to be 86 μs and 1.8 ms, respectively. The fast and slow decay times were 48 ms and 245 ms, respectively.[26] Mutagenesis studies found the slow opening and fast closing mechanism to be regulated by E68. The homologous residue in ChR2, E90, serves as an ion selectivity filter that, when mutated to a positive residue, turns ChR2 into a chloride conducting channel. Interestingly, in the E68R mutant of GtACR1 the channel was open in dark

state.[26] The fast opening, slow closing mechanism was found to be regulated by C102. Mutation to alanine resulted in a longer conductive state, 100-fold slower than WT. This variant is of interest and deserves further investigation as it has potential applications in therapies necessitating long lived conductance, including pain management.[27]

The photochemical reaction mechanism can provide additional understanding of the function of GtACR1 and its variants. The conventional naming system of the photointermediates in the mechanism are K, L, M, N, O, which are derived from the nomenclature used for BR. K is a red-shifted, early intermediate associated with the highly dipolar form of the retinal. O is also red shifted but appears later in the reaction. L, M, and N are all blue-shifted intermediates with M being the most significantly blue-shifted intermediate that is associated with the deprotonation of the Schiff base linked retinal. For BR, this deprotonation is coupled to the proton being translocated across the membrane.[28,29] Previous studies on the photomechanism of GtACR1 found the M intermediate appeared later than the onset of the current and ruled out the possibility of the M intermediate being the conductive state.[24] The formation of the M intermediate correlated temporally with the closing of the channel, contrary to ChR2, where the retinal Schiff base deprotonates before the channel opens.[2] An important question emerges of what photointermediate corresponds to the conductive, open-channel conformation.

Initial studies on the photocycle suggested that the open-channel intermediate of GtACR1 was the L-state as the only transition with kinetics in proximity to the

current rise was the K to L transition.[24] However, the formation of the L-intermediate occurs 10-100 times faster than the current rise time. Later time-resolved FTIR studies identified an additional transition within the time of the open channel and split the L intermediate into two distinct intermediates. This new transition was defined as L1 to L2, with L1 as an early non-conducting and L2 as the conducting intermediate.[17] Still, this new transition at ~2 ms did not coincide with the major component of channel opening at 86 μs.[26] So far no spectroscopic transition has been identified that is in agreement with the current rise from electrophysiology results.

1.5 Purpose of Thesis Project

The function of GtACR1 is intimately tied to its photochemical reaction mechanism in which the lifetime of conducting photointermediates dictate the channel conductance. GtACR1 is particularly advantageous for optogenetic applications as it has a 25-fold higher unitary conductance than ChR2 and can control neuronal inhibition with 1,000-fold higher sensitivity than any other silencing tool so far discovered.[11,30] The photoreactions of GtACR1 are investigated in this thesis through the lens of time-resolved absorption spectroscopy. Variants that showed unusual channel kinetics through *in-vivo* experiments are also explored. Knowledge of the open-channel photointermediate and explanations for unusual behavior of the variants provide additional means for more rational design of optogenetic tools.

1.6 References

1. Ostrovsky, M. A. Rhodopsin: Evolution and Comparative Physiology. *Paleontol. J.* **51**, 103–113 (2017).
2. Ernst, O. P. *et al.* Microbial and animal rhodopsins: Structures, functions, and molecular mechanisms. *Chem. Rev.* **114**, 126–163 (2014).
3. Guo, Z. V. *et al.* Flow of cortical activity underlying a tactile decision in mice. *Neuron* **81**, 179–194 (2014).
4. Lak, A. *et al.* Dopaminergic and prefrontal basis of learning from sensory confidence and reward value. *Neuron* **105**, 700-711.e6 (2020).
5. Etter, G. *et al.* Optogenetic gamma stimulation rescues memory impairments in an Alzheimer's disease mouse model. doi:10.1038/s41467-019-13260-9.
6. Liu, X. *et al.* Optogenetic stimulation of a hippocampal engram activates fear memory recall. (2012) doi:10.1038/nature11028.
7. Osawa, S. I. & Tominaga, T. Application of optogenetics in epilepsy research. *Adv. Exp. Med. Biol.* **1293**, 557–562 (2021).
8. McCarberg, B. & Peppin, J. Pain pathways and nervous system plasticity: learning and memory in pain. *Pain Med. (United States)* **20**, 2421–2437 (2019).
9. Sahel, J. A. *et al.* Partial recovery of visual function in a blind patient after optogenetic therapy. *Nat. Med.* **27**, 1223–1229 (2021).
10. Curtis, B. A. *et al.* Algal genomes reveal evolutionary mosaicism and the fate of nucleomorphs. *Nature* **492**, 59–65 (2012).

11. Govorunova, E. G., Sineshchekov, O. A., Janz, R., Liu, X. & Spudich, J. L. Natural light-gated anion channels: A family of microbial rhodopsins for advanced optogenetics. *Science (80-.).* **349**, 647–650 (2015).

12. Mauss, A. S., Busch, C. & Borst, A. Optogenetic neuronal silencing in Drosophila during visual processing. *Sci. Rep.* **7**, (2017).

13. Messier, J. E., Chen, H., Cai, Z. L. & Xue, M. Targeting light-gated chloride channels to neuronal somatodendritic domain reduces their excitatory effect in the axon. *Elife* **7**, 1–21 (2018).

14. Mohammad, F. *et al.* Optogenetic inhibition of behavior with anion channelrhodopsins. *Nat. Methods* **14**, 271–274 (2017).

15. Mahn, M., Prigge, M., Ron, S., Levy, R. & Yizhar, O. Biophysical constraints of optogenetic inhibition at presynaptic terminals. *Nat. Neurosci.* **19**, 554–556 (2016).

16. Li, H. *et al.* Crystal structure of a natural light-gated anion channelrhodopsin. *Elife* **8**, 1–21 (2019).

17. Dreier, M. A. *et al.* Time-resolved spectroscopic and electrophysiological data reveal insights in the gating mechanism of anion channelrhodopsin. *Commun. Biol.* **4**, (2021).

18. Yi, A., Mamaeva, N., Li, H., Spudich, J. L. & Rothschild, K. J. Resonance raman study of an anion channelrhodopsin: effects of mutations near the retinylidene Schiff base. *Biochemistry* **55**, 2371–2380 (2016).

19. Bruun, S. *et al.* Light-dark adaptation of channelrhodopsin involves

photoconversion between the all-trans and 13-cis retinal isomers. *Biochemistry* **54**, 5389–5400 (2015).

20. Kim, Y. S. *et al.* Crystal structure of the natural anion-conducting channelrhodopsin GtACR1. *Nature* **561**, 343–348 (2018).
21. Sineshchekov, O. A., Govorunova, E. G., Li, H., Wang, X. & Spudich, J. L. Opposite charge movements within the photoactive site modulate two-step channel closing in GtACR1. *Biophys. J.* **117**, 2034–2040 (2019).
22. Govorunova, E. G., Sineshchekov, O. A., Li, H. & Spudich, J. L. Microbial rhodopsins: Diversity, mechanisms, and optogenetic applications. *Annu. Rev. Biochem.* **86**, 845–872 (2017).
23. Luecke, H., Richter, H. T. & Lanyi, J. K. Proton transfer pathways in bacteriorhodopsin at 2.3 angstrom resolution. *Science.* **280**, 1934–1937 (1998).
24. Sineshchekov, O. A., Li, H., Govorunova, E. G. & Spudich, J. L. Photochemical reaction cycle transitions during anion channelrhodopsin gating. *Proc. Natl. Acad. Sci.* **113**, E1993–E2000 (2016).
25. Tsujimura, M., Kojima, K., Kawanishi, S., Sudo, Y. & Ishikita, H. Proton transfer pathway in anion channelrhodopsin-1. *Elife* **10**, 1–17 (2021).
26. Sineshchekov, O. A., Govorunova, E. G., Li, H. & Spudich, J. L. Gating mechanisms of a natural anion channelrhodopsin. *Proc. Natl. Acad. Sci.* **112**, 14236–14241 (2015).
27. Iyer, S. M. *et al.* Optogenetic and chemogenetic strategies for sustained inhibition of pain. *Sci. Rep.* **6**, (2016).

28. Lanyi, J. K. Proton transfers in the bacteriorhodopsin photocycle. *Biochim. Biophys. Acta - Bioenerg.* **1757**, 1012–1018 (2006).

29. Lanyi, J. K. Bacteriorhodopsin. *New Compr. Biochem.* **23**, 75–101 (2004).

30. Govorunova, E. G. *et al.* The expanding family of natural anion channelrhodopsins reveals large variations in kinetics, conductance, and spectral sensitivity. *Sci. Rep.* **7**, (2017).

CHAPTER 2

General Methodology of Materials Produced and Experiments Performed

2.1 Molecular biology methods

2.1.1 Plasmid and bacmid production

The gene for wild type GtACR1 purchased from Addgene and ligated with a C-terminal 8×His tag between the HindIII and EcoRI restriction sites in a pNT79i vector was kindly provided by Prof. Seth Rubin (UCSC). Ligation was verified by sequencing using p10-5' and p10-3' primers. Plasmid amplification was performed with DH5α *E. coli* cells and purified with QIAGEN prep kit graciously donated by Prof. Carrie Partch (UCSC). To generate recombinant bacmid, pNT79i-GtACR1 was transformed into DH10β *E. coli* cells via heat-shock and inoculated in lysogeny broth (LB) media for 24 hours. Cell cultures were then streaked on LB agar plates containing 50 μg/mL kanamycin, 7 μg/mL gentamicin, 10 μg/mL tetracycline, 100 μg/mL Bluo-gal, and 40 μg/mL isopropyl β-d-1-thiogalactopyranoside (IPTG). Plates were incubated for 3-4 days at 37 ºC and white colonies were selected and cultured in 6 mL LB plus the three antibiotics for 24 hours. Bacmid purification was performed with a modified miniprep protocol to improve yield of the large DNA construct.[1] Cells were spun down from 3× 6 mL overnight cultures and combined into one Eppendorf tube. All media was removed, and the pellet was resuspended in 0.2 mL of ice cold QIAGEN Resuspension Buffer (50 mM Tris-Cl, pH 8.0, 10 mM EDTA, 100 ug/mL RNase A). The resuspended pellet was incubated for 5 minutes at room temperature and 5 minutes on ice. Subsequently, 0.4 mL of ice cold QIAGEN Lysis Buffer (200 mM sodium hydroxide, 1% sodium dodecyl sulfate) was added and the solution incubated on ice for 5 minutes. subsequently, 0.3 mL of QIAGEN Neutralization Buffer (3.0 M potassium acetate, pH

5.5) was added, chilled at -80 ºC for 15 minutes, and then thawed to room temperature. The resulting sample was centrifuged at 12,000×g for 15 minutes at 4 ºC. The white precipitate was mixed with 0.5 mL ice cold isopropanol, chilled at -80 ºC for 15 minutes, thawed to room temperature, and centrifuged at 12,000×g for 20 minutes at 4 ºC. The next few steps were performed in a sterile tissue culture hood with Laminar air flow. The bacmid DNA pellet was washed with ice cold 70% ethanol, centrifuged to remove the ethanol, and dried with the tubes inverted for 15 minutes. The DNA was resuspended in sterile water aliquoted into separate tubes at a concentration of 1 μg/μl and stored at -80 ºC until transfection. No vortex mixing was performed during the mixing steps, only gently mixing (e.g. inverting the tube) was performed.

2.1.2 Tissue culture

Sf9 insect cells and ESF 921 cell culture media were purchased from Expression Systems. Cells were plated to a density of 2×10^6 cells/mL and transfected with TransIT-Insect Transfection Reagent (Mirus) in a TransIT-to-bacmid ratio of 2:1 (v/v). Suspension cells were grown to a density of 2×10^6 cells/mL and infected with P3 recombinant baclovirus at a virus-to-cell ratio of 1:20 (v/v). All-trans-retinal (ATR, Sigma) in ethanol was added for a final concentration of 5 μM at the start of the infection. Cells were incubated at 27 ºC in a spinner flask at 240rpm for 72 hours. *Pichia pastoris* integrant cells for the S97E, D234N, A75E, and C102A mutants were kindly gifted by Prof. John Spudich (The University of Texas Health Science Center at Houston). These cells were plated on yeast extract-peptone-dextrose (YPD) with 2

mg/mL geneticin (G418), graciously donated by Prof. Doug Kellogg (UCSC), for 3-4 days at 30 ºC. Single colonies were inoculated in a buffered glycerol-complex medium (BMGY) and grown until the optical density at 600 nm reached between 4-6. BMGY media was replaced with buffered methanol-complex medium (BMMY), and expression was induced with the addition of 1% methanol. Cultures were supplemented with ATR in methanol to a final concentration of 5 μM at the start of the expression and grown overnight (12-18 hours) at 30 ºC while shaking at 240 rpm. Harvested Sf9 and *P. pastoris* cells were pelleted in a Fiberlite F9-6 rotor at 4,000 rpm and stored at -80 ºC until purification.

2.1.3 Purification of channelrhodopsins

Cells were resuspended in lysis buffer containing 20 mM 4-(2-hydroxyethyl)-1-piperazineethanesulfonic acid (HEPES) at a pH of 7.4, 300 mM sodium chloride (NaCl), 5% glycerol, 0.1 mM phenylmethylsulfonyl fluoride (PMSF), and 1 mM ethylenediaminetetraacetic acid (EDTA). Sf9 insect cells were lysed using sonication at a frequency of 20 MHz, 10 seconds on and 40 seconds off for six cycles on ice at 4 ºC. P. pastoris cells were lysed using a French press with a pressure of ~15,000 psi and the cell press cooled to 4 ºC. All subsequent purification steps were identical for the two cell types. Lysed cells were centrifuged at 4 ºC at a low speed of 4,500×g for 10 minutes in an Eppendorf 5810R centrifuge and then at a high speed of 151,000×g, in a 70Ti rotor, for 1 hour in a Beckman Optima L-90K ultracentrifuge. The supernatant was discarded. The pellet was resuspended in 20 mM HEPES pH 7.4, 300 mM NaCl, 5% glycerol, 0.1 mM PMSF, and 1 mM EDTA, and homogenized with a glass Dounce

homogenizer, ~20 strokes, on ice. The homogenous mixture was then supplemented with 1% n-dodecyl-β-D-maltoside (DDM, Anatrace) and solubilized anywhere from 1 hour to overnight at 4 ºC while nutating. The solubilized solution was centrifuged at 151,000×g for 1 hour. Depending on the yield, the pellet process was repeated where the pellet from the second ultracentrifuge step was subsequently resuspended, homogenized, and solubilized with a total of 2% DDM for 1hr to overnight. This process was never repeated for a third time and the total DDM concentration for solubilization did not exceed 2%. The supernatant was incubated with Ni-NTA resin for 1 hour. Ni-NTA resin was equilibrated with 20 mM HEPES pH 7.4, 300 mM NaCl, 5% glycerol, 0.1 mM PMSF, 1 mM EDTA, and 0.03% DDM. The Ni-NTA resin was step-wise washed with the equilibration buffer supplemented with 20 mM and 40 mM imidazole. Each step was 20 column volumes. The protein was eluted with the same buffer supplemented with 400 mM imidazole. Buffer exchange and concentrating the protein were performed with a 30 KDa MWCO filter. For the buffer exchange, the protein was flushed with the appropriate buffer at least three times. Proteins were concentrated to at least 1 mg/mL, flash frozen in liquid nitrogen, and stored at -80 ºC for future experiments.

2.2 Experimental Methods

2.2.1 Steady-state absorption spectroscopy

Steady-state optical absorption measurements were carried out on a Jasco V-750 UV-Vis spectrophotometer in a 0.4 cm pathlength quartz cuvette. All steady-state measurements were performed with a baseline measurement of air. Most samples

exhibited scatter, which was subtracted using a linear combination Rayleigh scattering proportionalities $I_{scat} \propto \frac{1}{\lambda^4}$ for small particles and $I_{scat} \propto \frac{1}{\lambda^2}$ for larger particles.[2]

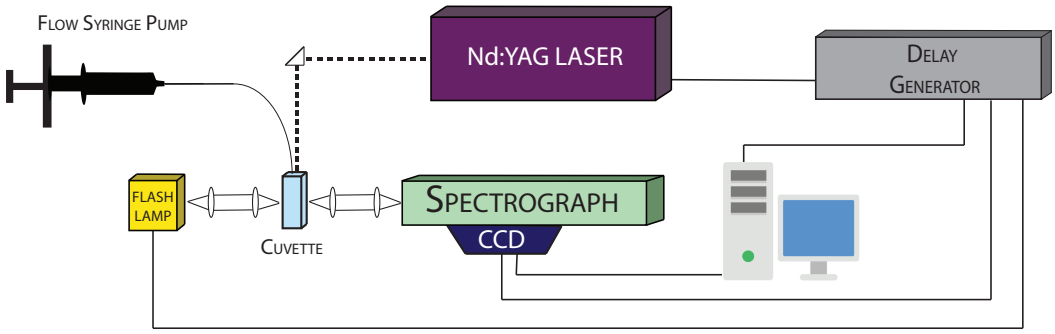

Figure 2.2.1: Diagram of the apparatus used to measure time-resolved absorption spectra.

2.2.2 Apparatus for time-resolved absorption spectroscopy

Time-resolved optical absorption experiments of GtACR1 and mutants were performed using 532 nm pulsed laser light (~7 ns full width at half maximum) from a Q-switched DCR-11 Nd:YAG laser for the pump. Probe pulses were produced with a xenon flash lamp. The spectra were detected with an ICCD detector (Andor technology) coupled to the pump-probe system via a delay generator (Stanford Research). A schematic of the experimental apparatus is shown in **Figure 2.2.1**. Measurements were recorded at 22 delay times, logarithmically spaced between 100 ns and 1 s. At each delay time, a minimum of 100 averages were recorded. All time-resolved optical absorption experiments were performed in a 0.4 cm pathlength quartz cuvette at room temperature. Fresh sample was injected in 10 µl aliquots into the cuvette before each measurement and recirculated to prevent any secondary photoexcitation.

2.2.3 Methods of analysis of time-resolved absorption data

The kinetics of a chemical reaction can be represented algebraically where the time dependence of each intermediate takes the form:

$$\frac{d[C_i(t)]}{dt} = \boldsymbol{K}[C_i(t)]$$

Here $[C_i(t)]$ is the concentration vector of all chemical species, $\frac{d[C_i(t)]}{dt}$ is the change in concentration over time, and $\boldsymbol{K}$ is the matrix of associated microscopic rate constants. The analysis of the experimental data requires a proposed kinetic matrix. The simplest first guess is the unidirectional sequential scheme

$$C_0 \overset{k_1}{\rightarrow} C_1 \overset{k_2}{\rightarrow} C_2 \overset{k_3}{\rightarrow} C_3$$

with a kinetic matrix, $\boldsymbol{K}$, as follows:

$$\boldsymbol{K} = \begin{pmatrix} -k_1 & 0 & 0 & 0 \\ k_1 & -k_2 & 0 & 0 \\ 0 & k_2 & -k_3 & 0 \\ 0 & 0 & k_3 & 0 \end{pmatrix}$$

The general solution to a set of first-order differential equations is a series of exponentials. For the set of kinetic rate equations, the general solutions is:

$$[C_i(t)] = \sum_n f_n \nu_n e^{\alpha_n t}$$

where α_n, the eigenvalues of $\boldsymbol{K}$, are the microscopic rates. ν_n are the eigenvectors and represent the intermediate states. f_n are scalar prefactors determined from the initial conditions.[4,6] For a unidirectional sequential scheme, the microscopic rates equal the observed rate constants. For all other schemes, the observed rate constants are a linear combination of eigenvalues.

Experimental data collected from time-resolved absorption measurements are the difference between post-excitation (A_f) and pre-excitation ($A_\circ$) absorption spectra at each wavelength (λ) and specified delay time (t_f).

$$\Delta A(\lambda, t) = A_f(\lambda, t_f) - A_\circ(\lambda, t_\circ)$$

Time-resolved absorption measurements were collected over a wide range of wavelengths with approximately 700 data points between 350-725nm. Each data point evolves over time and exponential fitting of 700 different curves would be computationally expensive. To reduce computation time, the data was reduced usinf singular value decomposition (SVD) before being approximated with a series of exponentials. SVD separates the data matrix, $\Delta A(\lambda, t)$, into spectral and time components

$$\Delta A = \mathbf{USV^T}$$

The decomposed matrices **U** and $\boldsymbol{V^T}$ are orthonormal. **U** contains the orthonormal basis spectra, **S** are the associated eigenvalues, and $\boldsymbol{V^T}$ is the transpose of the matrix containing the time evolution of the basis spectra. After decomposing the data matrix, an approximation is made by using a subset of the decomposed matrices for subsequent analysis. The approximation is based on the fact that only a finite number of terms describe the actual ongoing physical processes and additional terms are fitting experimental noise. Selection of the subset is determined from the **S** matrix, where the eigenvalue components describe the relative importance (i.e. weight) of each basis spectrum. The approximation is adequate when the square of the difference of the

actual data and the truncated representation is within experimental noise. The SVD approximation reduces noise and computational costs for the subsequent exponential fitting.[3–5]

For a first-order, or pseudo-first order reaction, the time dependence of the time-resolved absorption data (**V** , the matrix containing the time evolution of the **u**-spectra obtained from the decomposition) can be fit with a series of exponentials.

$$\Delta A(\lambda, t) = \sum_{n} b_n(\lambda) \exp(-r_n t) + b_\circ(\lambda)$$

n is the number of exponents used in the fitting, $b_n(\lambda)$ are called ***b***-spectra and represent the spectral change associated with an apparent lifetime, t. r_i are the observed rate constants where $r_n = 1/\tau_n$, and τ_n are the apparent lifetimes. $b_\circ(\lambda)$ will be explained later. The ***b***-spectra and apparent lifetimes do not represent physical processes. A kinetic scheme is necessary to connect the apparent lifetimes to the microscopic lifetimes, and the ***b***-spectra to the intermediate spectra. The eigenvectors of ***K*** are related to the ***b***-spectra through the extinction coefficients of the intermediate states, $\epsilon_n(\lambda)$.

$$\epsilon_n(\lambda) f_n \nu_n = b_n(\lambda)$$

K is a singular matrix, implying one of its eigenvalues is zero. The physical reason is due to the conservation of mass. The eigenvector associated with the zero eigenvalue is the time-independent state.[4]

$$b_\circ(\lambda) = \epsilon_\circ(\lambda)(f_\circ \nu_\circ) - A_\circ(\lambda, t_\circ)$$

In practice, one starts with the ***b***-spectra to calculate the eigenvectors and intermediates and then deduces a kinetic scheme. A proposed kinetic scheme is valid when the eigenvalues of the proposed kinetic matrix equal the apparent rates from the experimental data, and the intermediate spectra from the scheme reproduces the experimental ***b***-spectra. The calculated intermediate difference spectra are the absorption difference between pre- and post-excitation. Addition of the steady-state spectrum, $A_{\circ}(\lambda, t_{\circ})$, to the intermediate spectra produces the absolute intermediate spectra. Furthermore, the relative fractional concentration of each intermediate present at time, t, can be determined from the composition of the unique intermediates at a given time. Most microbial rhodopsins, including the anion channelrhodopsin from *Guillardia theta*, have a cyclic photochemical reaction. For a cyclic photochemical reaction where the initial state is recovered at the end of the reaction, the time-independent state is theoretically the same as the initial state. ***K***, the kinetic matrix will reflect a cyclic reaction with off-diagonal terms.

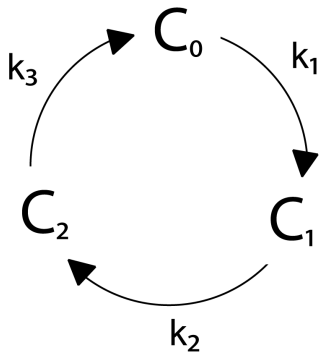

$$\boldsymbol{K} = \begin{pmatrix} -k_1 & 0 & k_3 \\ k_1 & -k_2 & 0 \\ 0 & k_2 & -k_3 \end{pmatrix}$$

2.3 References

1. Invitrogen. Bac-to-Bac® Baculovirus Expression System. *User Guid.* 1–78 (2015).

2. Krupka, R. M., Kaplan, H. & Laidler, K. J. Kinetic consequences of the principle of microscopic reversibility. (1966).

3. Thorgeirsson, T. E., Lewis, J. W., Wallace-Williams, S. E. & Kliger, D. S. Effects of pH on rhodopsin photointermediates from lumirhodopsin to metarhodopsin II. *Biochemistry* **37**, 6998–7005 (1998).

4. Szundi, I., Lewis, J. W. & Kliger, D. S. Deriving reaction mechanisms from kinetic spectroscopy. Application to late rhodopsin intermediates. *Biophys. J.* **73**, 688–702 (1997).

5. Szundi, I. *et al.* Platymonas subcordiformis channelrhodopsin-2 function: I. The photochemical reaction cycle. *J. Biol. Chem.* **290**, 16573–16584 (2015).

6. Millhauser, G. L. & Oswald, R. E. A reevaluation of the mathematical models for simulating single-channel and whole-cell ionic currents. *Synapse* **2**, 97–103 (1988).

CHAPTER 3

Elucidation of the Kinetics and Mechanism of the Wild- Type Channelrhodopsin from *Guillardia theta:*

Time-Resolved Absorption Spectroscopic Studies

3.1 Introduction

The two anion channelrhodopsins (ACRs) from *Guillardia theta* (*G. theta*) were discovered in 2015 through a Basic Local Alignment Search Tool of the cryptophyte alga's genome.[1] ACRs are proposed to be responsible for phototaxis and photophobic behavior, as *G. theta* is known to track the direction of light stimulus.[2–4] Both ACRs naturally conduct chloride ions in native conditions but can conduct other anions when expressed in non-native cells.[5] The passive channel function of channelrhodopsins allows control of cellular membrane potential through optogenetics.[6] Passage of anions across neuron membranes inhibits activity. The ACRs from *G. theta* have been shown to inhibit activity and control behavior in a wide range of living animals.[7–10] Of the two anion channelrhodopsins from *G. theta*, only GtACR1 is known to maintain its ion conductance *in vitro.*[11] GtACR1 is particularly advantageous for optogenetic application as it can control neuronal inhibition with a 10,000-fold higher sensitivity than any other silencing tool so far discovered.[1,5] Additionally, GtACR1 has a 25-fold higher unitary conductance than the most widely used optogenetic tool, the cation channelrhodopsin from *Chlamydomonas reinhardtii*. A more complete picture of the functional mechanism is necessary to understand the exceptionally high conductance and facilitate the design of molecular tools for optogenetic applications.

The structure of GtACR1 consists of a seven α-helix transmembrane domain with all-trans-retinal attached through a Schiff bond linkage to a lysine on the middle of the seventh helix.[11,12] The protein exists as a dimer through an interdomain disulfide

bond linkage.[12] Consistent with other microbial rhodopsins, GtACR1 undergoes a photoisomerization from the trans configuration to cis, which triggers a cascade of conformational changes for the protein. For GtACR1 and other channelrhodopsin variants, these conformational changes include the opening of a channel that permits the passage of ions across the lipophilic membrane. The channel is formed between the first, second, third, and seventh transmembrane helices.[11,12]

The channel kinetics can be monitored *in vivo* through whole-cell patch clamp electrophysiology. Electrophysiology experiments under single turnover conditions, where no secondary photoexcitation occurs, revealed two distinct channel mechanisms, one involving a fast rise and slow decay, and the other a slow rise and fast decay.[13] The fast and slow rise times were reported to be 86 μs and 1.8 ms, respectively. The fast and slow decay times were 48 ms and 245 ms, respectively.[13]

The ion transport of GtACR1 is intimately tied to its photochemical reaction mechanism in which the lifetimes of open-channel photointermediates dictate the channel conductance. The conventional naming system of the photointermediates are K, L, M, N, O, and they are derived from the earliest studied haloarchaeal proton pump bacteriorhodopsin. K is a red-shifted early intermediate associated with the highly dipolar form of retinal. M is the blue-shifted intermediate associated with the deprotonation of the Schiff base linked retinal. For bacteriorhodopsin, this deprotonation is coupled to the proton being translocated across the membrane.[14,15]

Previous studies on the photomechanism of GtACR1 found that the M intermediate appeared later than the onset of the current, which ruled out the possibility

of the M intermediate being the conductive state.[16] Instead it was suggested that the open-channel intermediate was the L-state as the current rise time occurred somewhere during the K to L transition. The proposed mechanism does not explain the electrophysiological results. For example, the authors define the conducting state occurring during the K → L transition despite the formation of the L-intermediate occurring 10-100 times faster. A better justified photomechanism is necessary to understand the functional properties of GtACR1.

3.2 Materials and Methods

The materials and methods were previously described in **Chapter 2**. For WT pH 7.5, a total of 500 time-resolved optical absorption spectroscopic measurements were taken for each of the 22 delay times. These measurements were taken on five separate days for three distinct samples. For WT samples at pH 5.5, 6.5, and 8.5 a total of 100 measurements were taken at each pH on one sample. For WT GtACR1 with bromide, a buffer exchange was performed with 350 mM NaBr used in the buffer instead of NaCl using a 30 KDa molecular weight cutoff filter. A total of 200 time-resolved optical absorption measurements were taken on WT GtACR1 with bromide. For the S97E mutant in pH 7.5 buffer, 350 measurements were taken over three days on two distinct samples. For each condition, all measurements were combined and averaged before subsequent analysis.

3.3 Results and Discussion

3.3.1 Uncovering the Spectral Forms of Wild-Type Under Standard Conditions

Figure 3.3.1 shows the absorption spectrum of wild-type GtACR1. GtACR1 in the ground state of the dark adapted protein contains only the all-trans configuration of retinal attached to a conserved lysine (K238) through a protonated Schiff base.[17] In this work, the dark form and ground form will be used synonymously to represent the ground state of the dark adapted protein. The main band for free all-trans-retinal in methanol is at 390 nm and the free protonated all-trans-retinal Schiff base is at 440 nm.[18,19] The main band of the chromophore in GtACR1 is at 515 nm (figure 3.3.1). The red shift of the protonated dark form of GtACR1 compared to free all-trans-retinal occurs due to the protein stabilizing the resonance of the positive charge far from the amide linkage around the ionone ring; this is commonly referred to as the opsin shift.[20] The peak in the near-UV around 280 nm is from the aromatic residues.[21]

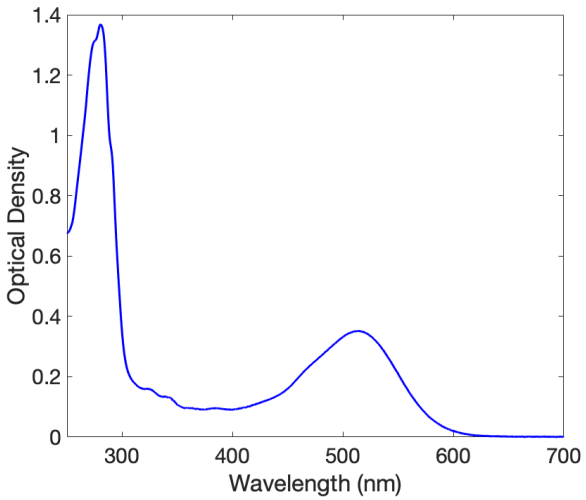

Figure 3.3.1: Absorption spectrum of the dark form of WT GtACR1 in 20 mM HEPES (pH 7.5) buffer with 300 mM NaCl, 5% glycerol, and 0.03% DDM.

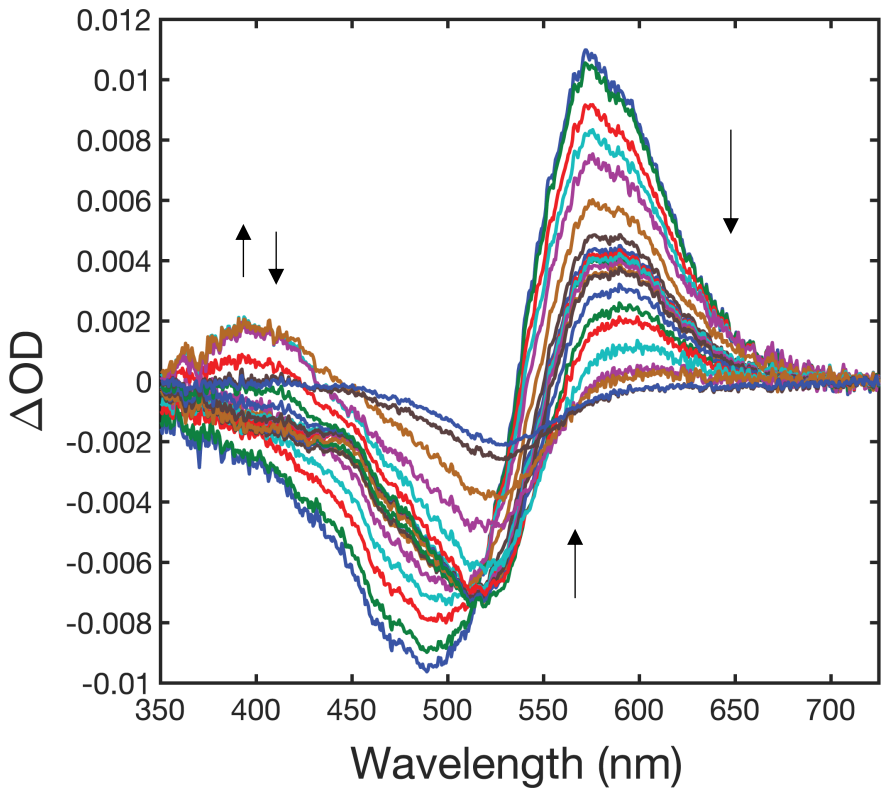

Figure 3.3.2: Time-resolved optical absorption difference spectra (post- minus pre-excitation) of the wild-type anion channelrhodopsin in 20 mM HEPES (pH 7.5) buffer with 300 mM NaCl, 5% glycerol, and 0.03% DDM. The difference spectra were recorded at 22 logarithmically spaced time points from 100 ns to 1 s.

Time-resolved optical absorption spectroscopy was performed on WT GtACR1 with a pump pulse at 532 nm to selectively excite the main band of the protonated all-trans-retinal Schiff base in GtACR1. **Figure 3.3.2** is the time-resolved optical absorption difference spectra of WT GtACR1 recorded between 350 to 750 nm at 22 logarithmically space time points from 100 ns to 1 s. The positive band at 575 nm is associated with a spectral form that is red-shifted relative to the dark form. The arrow describes a decay of this feature from 100 ns to 1 s. This red-shift is associated with the highly dipolar form of retinal in the excited state interacting with the electrostatics of

the chromophore binding pocket in a way that stabilizes the positive charge far from the Schiff base amide.[20,22] The negative band at 515 nm is the ground state bleach. This negative signal persists until the end of the experiment, as observed in the non-flat final difference absorption at 1 s, and indicates a small population that does not fully recover to the ground state of the dark form but remains in a closely related recovered state. This has also been observed for other channelrhodopsins.[23] The arrow defines the direction of this feature over the entire time range of this experiment. The positive peak at 390 nm is associated with a blue-shifted spectral form that is observed when the Schiff base becomes deprotonated.[24] The feature starts to appear at the 5 ms delay time and then decays starting at the 100 ms delay time, which is illustrated in the figure by the up and down arrows.

The time-resolved optical absorption difference spectra were analyzed using SVD and exponential fitting (see **Chapter 2** – General Methods for information on SVD and global exponential fitting). **Figure 3.3.3** shows the results of the first SVD. **Figure 3.3.3.C** is the significance values of each **u**,**v**-vector pair where **u** is the orthonormal basis spectra and **v** is the time-evolution of its associated **u**. The significance values indicate that the first four vector pairs were necessary to reproduce the data with significant values of 0.3857, 0.1273, 0.0326, and 0.0180, respectively. The other pairs contain experimental noise only. The **u**-vectors and their time evolution are depicted in in **Figure 3.3.3 A** and **B**, respectively. The **u**-vectors in **Figure 3.3.3.A** also illustrate the necessity for four **u**-spectra as the shapes resemble spectral shapes instead of random noise.

The time-evolution of the **u**-spectra was first fit with a series of four exponentials. The exponentials produced apparent lifetimes of 575 ns, 6.94 μs, 21.8 ms, and 187.4 ms. The quality of the fit is assessed through a number of means, including an evaluation of the ***b***-spectra. **Figure 3.3.4.A** depicts the spectral changes, or ***b***-spectra, at each apparent lifetime. The positive peaks represent spectral forms decaying and the negative troughs are the forms appearing at the specified lifetime. There are no outliers or divergent symmetric forms with lifetimes within the same decade, a marginal indication of an adequate fit. However, increasing the exponentials in the series to greater than four did produce divergent ***b***-spectra. The residual plot in **Figure 3.3.4.B** compares the data reproduced from the fit with the raw data for each delay time. There are some noticeable changes between the reproduced spectral shapes and the fit as revealed from the skewed lines. The temporal evolution is the most important means to asses fitness quality. **Figure 3.3.4.C** shows the **v**-vectors from the SVD truncation (dots) with the reproduced vectors from the exponential fit (solid lines). Deviations in the green and red vectors (solid lines) are quite pronounced at later times. These deviations are furthered illustrated in **Figure 3.3.4.D** where the difference between the **v**-vectors and fit at later times are more than the random noise of the experiment, indicating the 4- exponential fit is unsatisfactory.

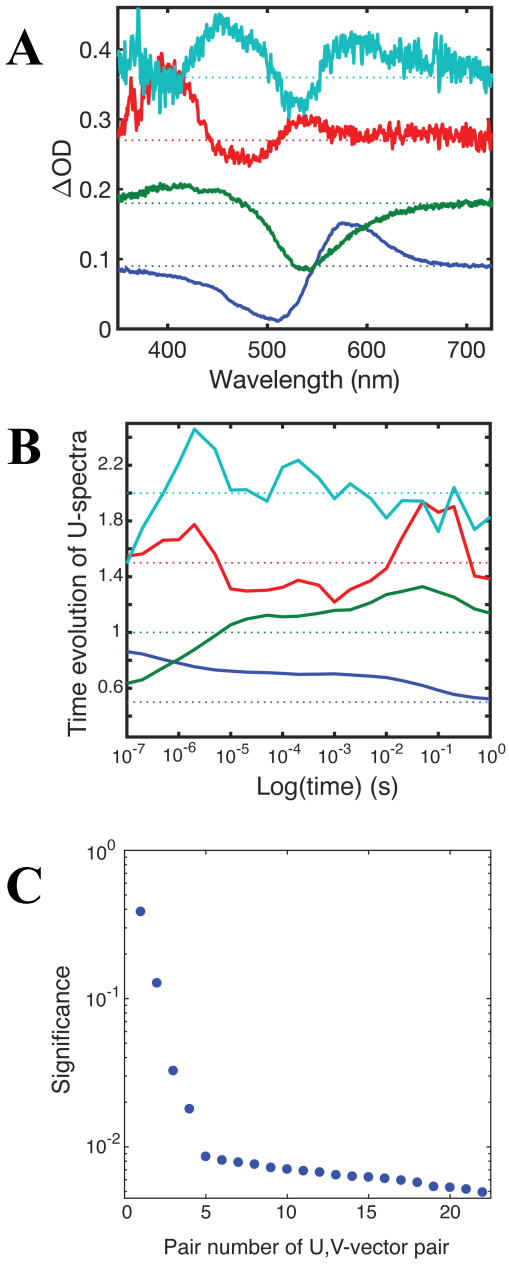

Figure 3.3.3: (A) Orthonormal basis spectra (**u**-spectra) of the first fit. (**B)** The time evolution of the **u**-spectra, called the **v**-vectors. (**C**) Significance values of each **u**,**v**-vector pair. The first four **u**,**v**-vector pairs are much more significant with values of 0.3857, 0.1273, 0.0326, and 0.0180, respectively.

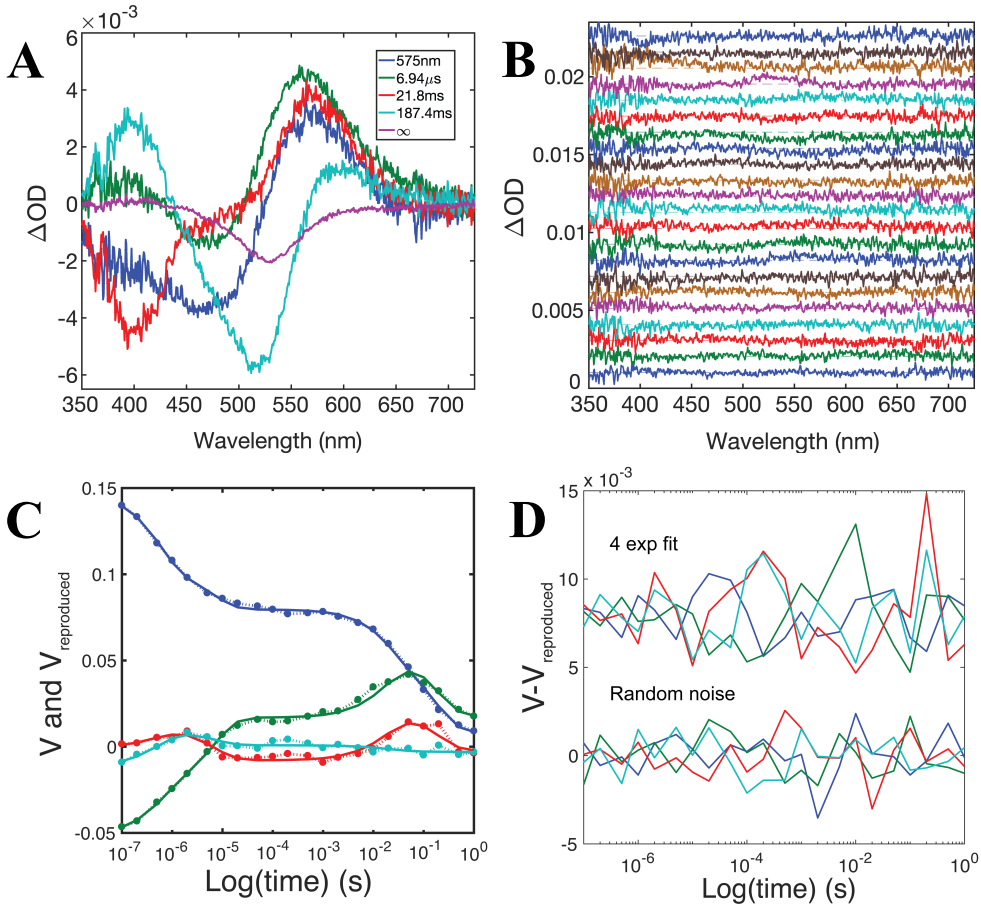

Figure 3.3.4: (A) The spectral changes, ***b***-spectra, for each apparent lifetime from the 4-exponential fit of the time-resolved optical absorption data of WT GtACR1. The legend illustrates the apparent lifetime associated with each ***b***-spectrum with ∞ being $\boldsymbol{b}_\infty(\lambda)$, the ***b***-spectrum associated with the time-independent state. **(B)** The spectral residuals of the fit compared to the data for each delay time (increasing from bottom to top from nanoseconds to seconds). **(C)** The significant **v**-vectors determined from the SVD of the difference spectra (dotted lines) compared to the reproduced vectors of the five-exponential fit (solid lines). **(D)** The temporal residuals (data minus fit) for the 4-exponential fit contrasted with the level of random noise produced from the experiment. The fit does not reproduce the data within the experimental noise.

To overcome the unsuitable fit, important adjustments were made to the raw data. The experimental apparatus for this study involves a xenon arc flash lamp that can exhibit changes in intensity when the arc moves and as a result of temperature changes, the result of which is an inevitable tilt in the baseline.[25] This tilt can be observed in the spectral residuals in **Figure 3.3.3.B**. Additionally, early delay times, 100 and 200 ns, produced negative tilts around 350 nm. This phenomenon is explained by thermal lensing from a black metal insert in the cuvette producing non-negligible temperature gradients when interacting with the 10 mJ laser pulse. As the spectral changes in these TROD experiments are quite small, on the order of tens of mOD, a modest tilt in the baseline can produce an unsuitable data for exponential fitting. The datasets were corrected using a linear relationship of the tilt with wavelength. **Figure 3.3.5** is the corrected data set for the WT protein at neutral pH.

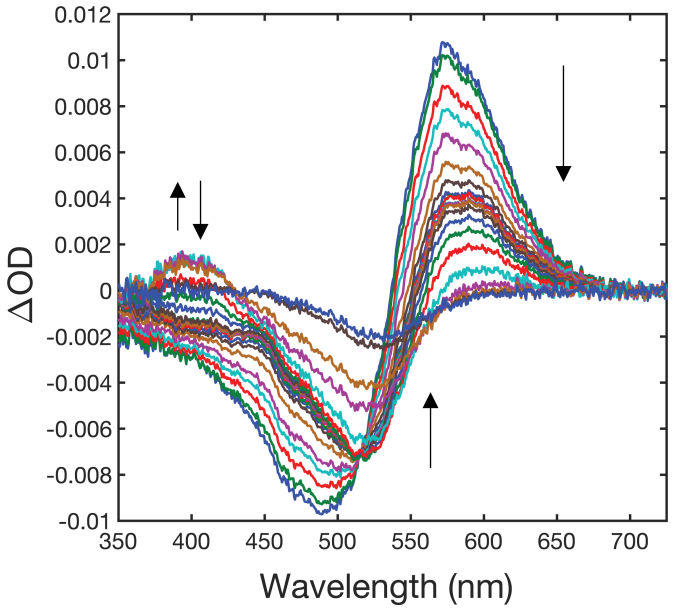

Figure 3.3.5: Time-resolved optical absorption data of WT after correcting for baseline tilt.

The tilt corrected data were decomposed into spectral and temporal components using SVD. **Figure 3.3.6** shows the SVD results. The significance values of the first four **u**,**v**-vector pairs are 0.3937, 0.1288, 0.0265, and 0.0087, respectively. Contrasting with the raw data, the significant value of the fourth **u**-spectrum (cyan) is now an order of magnitude less than for the uncorrected data. The **u**-spectra are presented in **Figure 3.3.6.B**. The shape of the fourth **u**-spectrum has the shape of random noise. Together the shape and significance value of the fourth **u**-spectrum indicate that, after the tilt correction, the data can be approximated with three **u**,**v**-vector pairs. **Figure 3.3.6.C** displays the time evolution of the spectral components (**v**-vectors). The time evolution was fit to a series of exponentials. Contrary to the raw data, any number of exponentials can be used to fit the **v**-vectors from the tilted data, without the occurrence of divergent ***b***-spectra. Similar to the raw data, fitting with 4 exponentials did not reproduce the data within experimental noise. **Figure 3.3.7** shows the **v**-vectors with a five and six-exponential fit (**Figure 3.3.7.A**) and the residuals between the **v**-vectors and the fit (**Figure 3.3.7.B**). The 5-exponential fit reproduced the data within the experimental noise. However, the shapes of the residuals did not resemble random noise, but had some wave-like structure. The 6-exponential fit also reproduced the data well within the experimental noise and the shapes of the residuals resembled random noise.

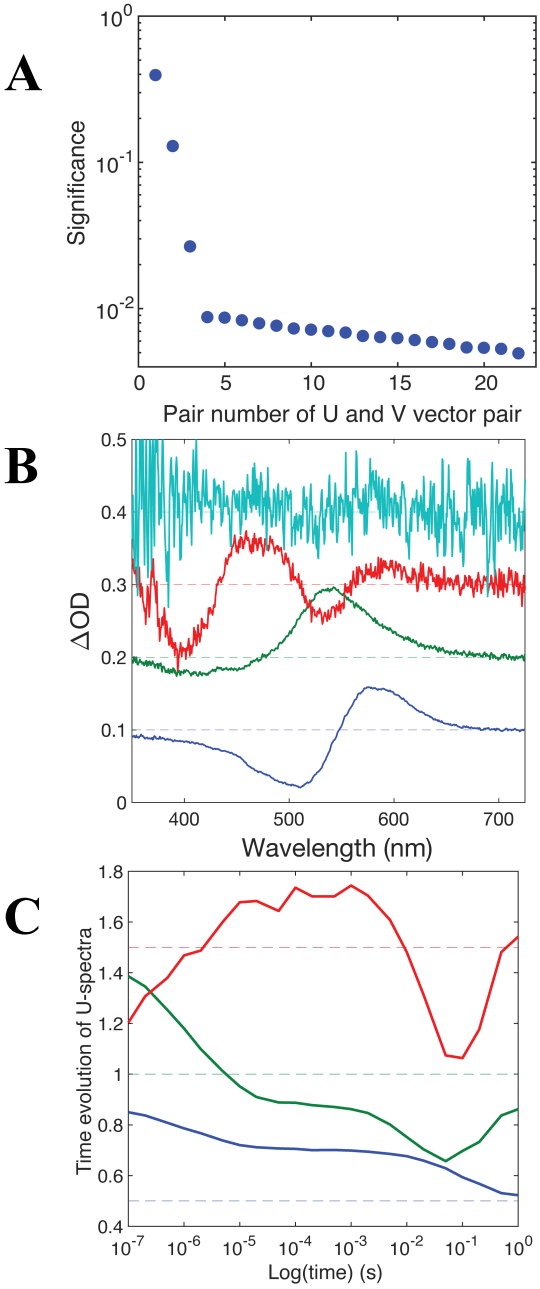

Figure 3.3.6: SVD of the tilt corrected data. **(A)** Significance values of the **u**,**v**-vector pairs. The significance values of the first four **u**,**v**-vector pairs are 0.3937, 0.1288, 0.0265, and 0.0087, respectively, where the last significant value is now an order of magnitude less than the previous. **(B)** The first four **u**-spectra. The fourth **u**-spectrum (cyan) has the shape of noise. This shape together with the low significant value specify a need for only three **u**,**v**-vector pairs to approximate the data. **(C)** The time evolution of the **u**-spectra (**v**-vectors).

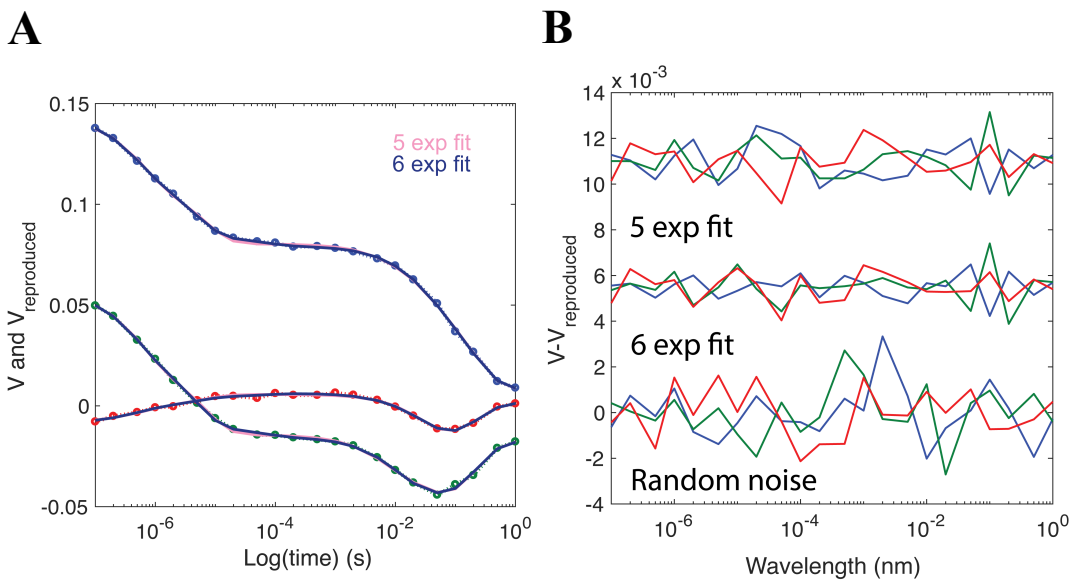

Figure 3.3.7: (A) The significant **v**-vectors determined from the SVD of the difference spectra (dots) compared to the reproduced vectors of the 5-exponential fit (solid pink lines) and the 6-exponential fit (solid blue lines). **(B)** The temporal residuals (data minus fit) for the 5-exponential and 6-exponential fits contrasted with the level of random noise produced from the experiment. While the 5-exponential fit does reproduce the data within the experimental noise, the temporal residuals have wave-like shapes.

The spectral changes produced from the 5-exponential and 6-exponential fits are presented in **Figure 3.3.8 A** and **B**, respectively. The 6-exponential fit revealed a minor component (red) in the hundreds of microseconds region. The other components appear relatively the same between the two fits. The residuals for the 5-exponential and 6-exponential fits are in **Figure 3.3.8 C** and **D**, respectively. The observed tilts and wave-like structures in the spectral residuals of the WT were remedied with the corrected data. The spectral residuals for the 5-exponential and 6-exponential are both satisfactory. Since the temporal residuals were superior for the latter, the analysis was carried out using the 6-exponential fit.

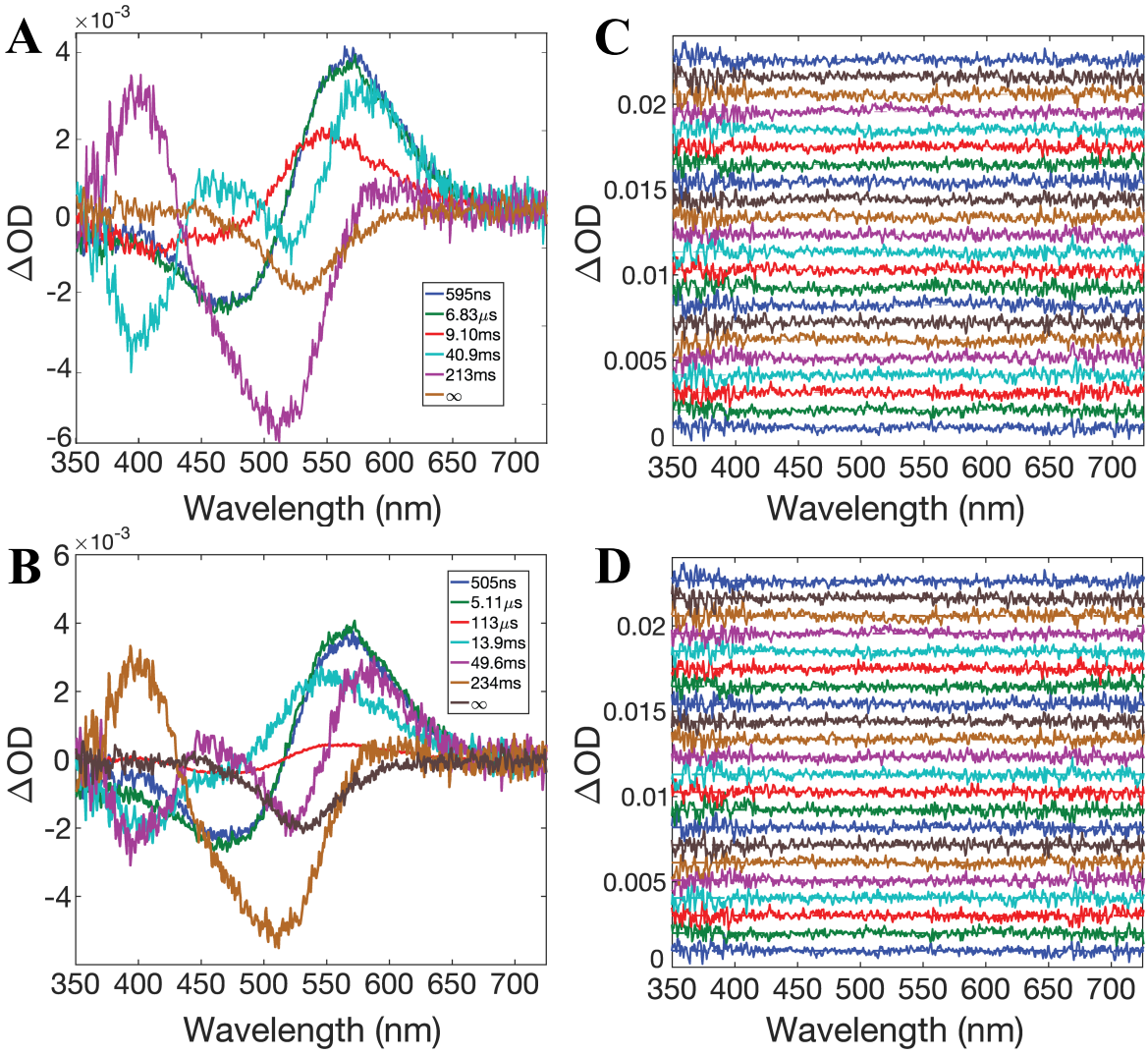

Figure 3.3.8: The spectral changes, also referred to as ***b***-spectra, for the 5-exponential **(A)** and 6-exponential **(B)** fits. The spectral residuals for each delay time (increasing from bottom to top from nanoseconds to seconds) for the 5-exponential **(C)** and 6-exponential **(D)** fits.

A kinetic scheme is necessary to connect the apparent lifetimes to the microscopic lifetimes, and the ***b***-spectra to the intermediate spectra.[23,26] The first proposed scheme is always the unidirectional sequential scheme. **Scheme 1** depicts this simple scheme with each of the apparent lifetimes in ascending order.

$$\mathbf{Int1} \xrightarrow{505ns} \mathbf{Int2} \xrightarrow{5.11\mu s} \mathbf{Int3} \xrightarrow{113\mu s} \mathbf{Int4} \xrightarrow{13.9ms} \mathbf{Int5} \xrightarrow{49.6ms} \mathbf{Int6} \xrightarrow{234ms} \mathbf{Int7}$$

Scheme 1: Unidirectional sequential scheme of the photomechanism of GtACR1.

Figure 3.3.9 illustrates the intermediate difference spectra assuming a straight unidirectional sequential scheme. Here, the positive peaks are the populations present and the negative troughs are the depleted populations at the given lifetime. All of the sequential intermediates contain a mixture of molecular intermediates with the most prominent being Int5 and Int6 where both red- and blue-shifted peaks are present. A red-shifted component persists throughout the entire experimental temporal range. Long-lived red-shifted intermediates have been observed in other channelrhodopsins and can indicate a fast early equilibrium between different states.[23] The blue-shifted deprotonated state, denoted M, shows up much later than in other microbial rhodopsins; detergent purification has been ruled out as the cause for a slow M-formation.[16]

To determine the number of true intermediates, we have to assume the shape of the intermediate spectra. This is fairly straightforward for retinal proteins where the intermediate spectra all have similar shapes when plotted on an energy (wavenumber) scale.[23] The process of determining these spectral forms follows procedures developed for determining the photomechanism of the cation channelrhodopsin.[23]

Figure 3.3.10 shows the absolute spectra of the decomposition of the sequential intermediates. The blue curve is the first, red-shifted intermediate after the addition of the bleach. The first intermediate of rhodopsins is known to be broader than the rest. This is due to the increased vibrionic degrees of freedom that comes from the stabilized positive charge far from the Schiff base amide.[20] The green, red, magenta, cyan, and mustard curves are the second, third, fourth, fifth, and sixth intermediates, respectively. Each of these intermediates contain some amount of the first, red-shifted intermediate as is apparent from **Figure 3.3.9**. Subtraction of the red-shifted intermediate and subsequent addition of the bleach resulted in intermediates 2 to 6 having the same spectral shape. Intermediate 5 and 6 also contained the blue-shifted M-intermediate not shown in **Figure 3.3.10**. Using the general rule of similar shapes, we know the decomposition is satisfactory when the spectral forms overlay the spectrum of the dark form (black curves) on the energy scale. From the decomposition, four unique spectral forms were determined. It didn't matter whether 4, 5, or 6 exponentials were used in the global fitting, the same four spectral forms were resolved. **Table 3.1** characterizes the amount of each spectral form in the sequential intermediates.

Figure 3.3.11 A shows the four unique absolute spectral forms. We call the first red-shifted intermediate K. The second intermediate that forms from the decay of K in the photochemical process is named L. The decomposition of the sequential intermediates revealed many L forms contained in the spectra. Addition of more than four terms in the exponential fitting of the **v**-vectors only revealed more L intermediates.

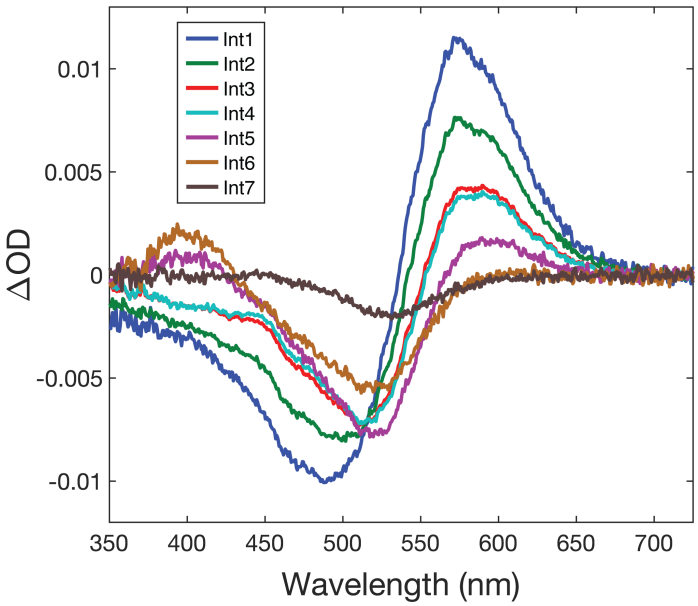

Figure 3.3.9: Difference spectra of the intermediates from the sequential scheme for wild-type GtACR1.

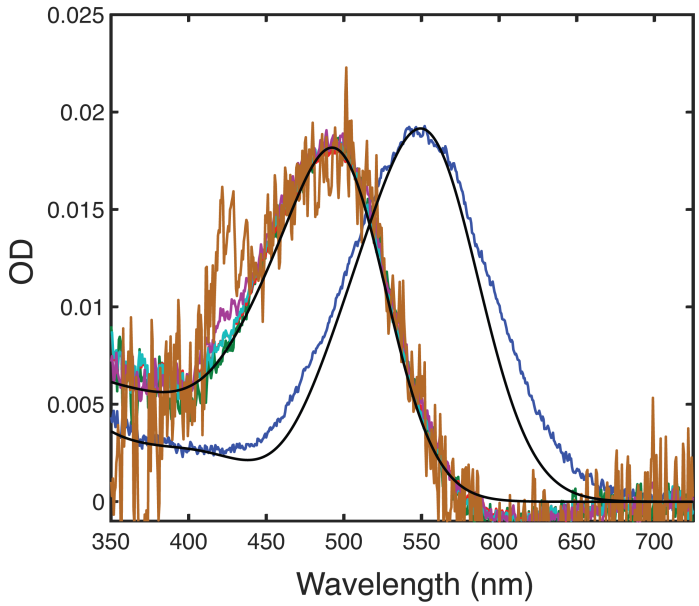

Figure 3.3.10: Unique spectral forms from decomposition of sequential intermediates. The black curves are the dark form spectrum wavelength shifted to overlay the decomposed intermediates. The blue curve is the first, red-shifted spectral form. The green, red, magenta, cyan, and mustard curves are the second, third, fourth, fifth, and sixth spectral forms, respectively. The M and recovered forms are not shown.

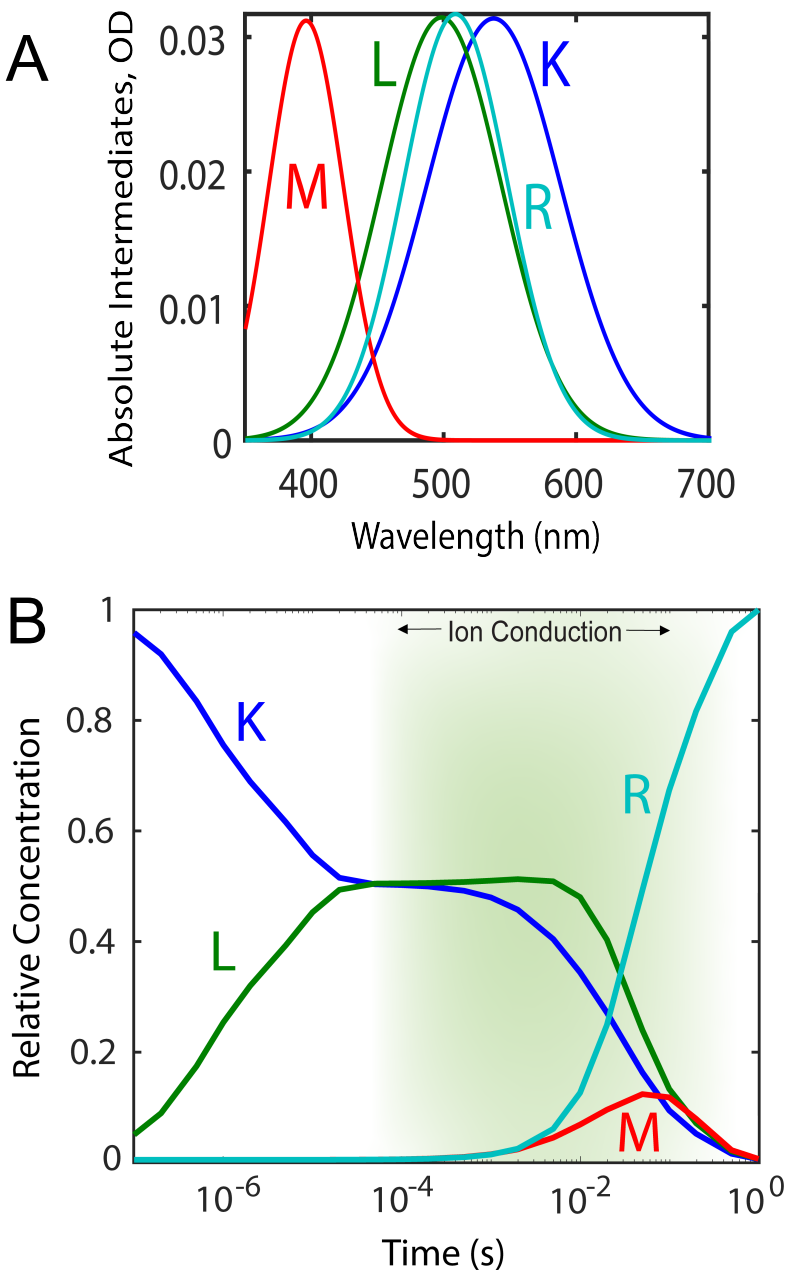

Figure 3.3.11: (A) Absolute intermediate spectral forms determined from decomposing the sequential intermediates into distinct spectra with similar shapes on the energy (wavenumber) scale. **(B)** Time dependent concentration profiles of the absolute intermediate spectral forms for WT GtACR1. The green highlighted time window is the region of ion conduction as determined from whole cell patch clamp electrophysiology measurements under single turnover conditions. (ref 13)

Form	SeqInt1	SeqInt2	SeqInt3	SeqInt4	SeqInt5	SeqInt6	SeqInt7
K	1	0.76	0.54	0.52	0.31	0.08	0
L	0	0.24	0.46	0.48	0.47	0.1	0
M	0	0	0	0	0.1	0.14	0
R	0	0	0	0	0.12	0.68	1

Table 3.1: Fractional composition of the spectral forms, K, L, M, and R within the intermediates from the sequential scheme for WT GtACR1.

Also formed during the course of the reaction was the blue-shifted deprotonated intermediate, called M, and the recovered form, called R. **Figure 3.3.11 B** shows the time-dependent concentration profiles. As observed with the sequential intermediates, the red-shifted K-like intermediate spectral form is present for the entire length of the temporal window. The L-like intermediate spectral form is also present for the entire experiment. It is highly unlikely these transient intermediate forms would exist individually for the length of the experiment that was carried out at room temperature nor do the shapes of the concentrations correspond to what one would expect of a specific chemical species. There is a chance that the individual forms contain a superposition of many forms. Additionally, there is no clear intermediate corresponding temporally to the open-channel state as determined from the time-dependent photocurrent observed in whole-cell patch-clamp electrophysiology experiments under single turnover conditions.[16] One possible explanation for the lack of an intermediate corresponding to the open-channel state is the existence of isospectral intermediates. Isospectral intermediates occur when more than one intermediate has the same spectral shape and appear close in time. This can be observed

as one extremely long-lived intermediate spectral form that is actually a superposition of more than one form. Additional evidence that supports the hypothesis of the existence of isospectral intermediates is the occurrence of more apparent lifetimes than spectral forms. The exponential fits with five and six apparent lifetimes only extracted four unique spectral forms. This hints at a loss of spectral information, or rank of the spectral matrix, from the fitting process. In other words, this indicates the presence of intermediates that are not detectable in this experiment, including an intermediate clearly corresponding to the open-channel configuration. To probe this hypothesis, the environmental bath conditions were modified in an attempt to resolve additional intermediates.

3.3.2 Effects of pH on time-resolved optical absorption difference spectra

To investigate the possibility of additional intermediates, the time-resolved absorption was measured for WT GtACR1 at various pHs. The absorption spectra of WT GtACR1 at pH 5.5 (blue), 6.5 (green), 7.5 (red), and 8.5 (cyan) are shown in **Figure 3.3.12**. The spectra overlay over this pH range and are in agreement with the literature.[16] The time-resolved optical absorption difference spectra for WT GtACR1 in the pH region specified above are shown in **Figure 3.3.13**. While the absorption spectra exhibit no change over this pH range, the time-resolve absorption changes show a clear distinction in the band at 400 nm (**Figure 3.3.13)**. This band is associated with

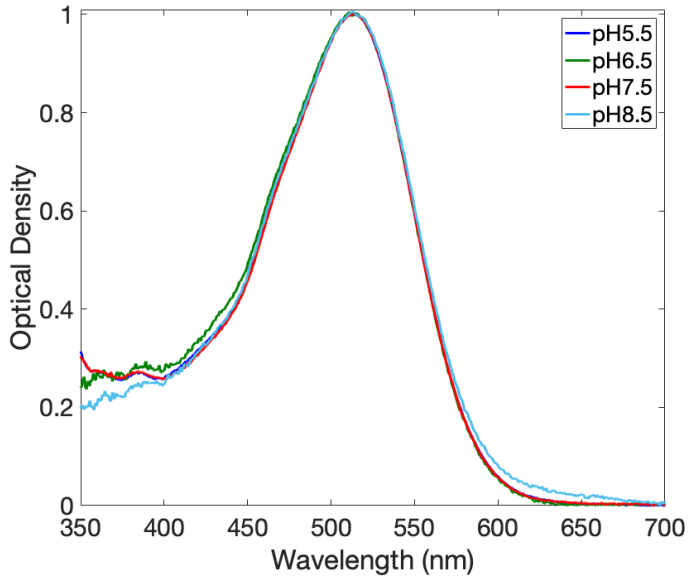

Figure 3.3.12: Absorption spectra of WT GtACR1 in pH 5.5 (blue), 6.5 (green), 7.5 (red), and 8.5 (cyan). Each sample was suspended in 20 mM HEPES with 300 mM NaCl, 5% glycerol, and 0.03% DDM. The pH was adjusted with NaOH and HCl.

the blue-shifted intermediate M and identifies the deprotonation of the Schiff base retinal. Global fitting of the pH 5.5, 6.5, and 8.5 data was performed using five exponentials. The lifetimes of the fits always included two fast components, ~0.5 µs and ~5 µs, and two slow components, ~20-50 ms and ~500 ms. The fifth lifetime varied between 100 µs-10 ms and was related to a minor component that was necessary for the fit. Similar to WT at pH 7.5, decomposition of the sequential intermediates produced four unique spectral forms. The time evolution of the spectral forms for each bath pH are displayed in **Figure 3.3.14**. Over the pH range investigated, the K and L forms exist for the duration of the experiment. The relative concentration of the M intermediate increases with increasing pH. This is expected as the M intermediate corresponds to the deprotonated

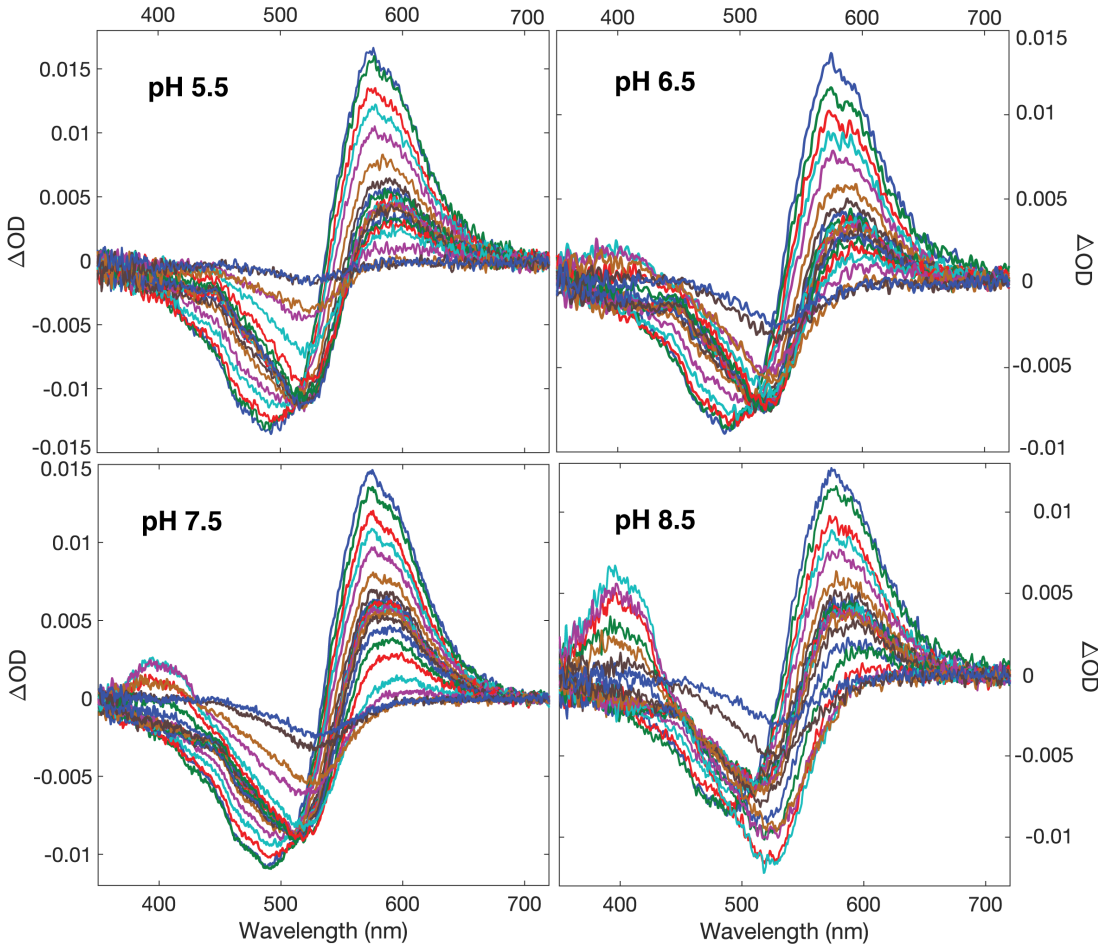

Figure 3.3.13: Time-resolved optical absorption spectra (post- minus pre-excitation) of WT GtACR1 in pH 5.5, 6.5, 7.5, and 8.5. Each sample was suspended in 20 mM HEPES with 300 mM NaCl, 5% glycerol, and 0.03% DDM. The pH was adjusted with NaOH and HCl. The difference spectra were recorded at 22 logarithmically spaced time points from 100 ns to 1 s.

the M form appearing only upon the decay of an L state.[16,27] These data define a clear transition from the K spectral form to M at pH 8.5. This pathway would be possible at any pH, and the simultaneous decay of the K form with the rise of M at the other pHs support this notion.

3.3.3 Substrate effects on time-resolved optical absorption spectra

Recent structural studies on the bromide bound GtACR1 found a pre-activated configuration that was not present in the chloride bound structure.[28] This pre-activated structural form may coincide with a change in the kinetics and may help resolve additional photointermediates. The time-resolved optical absorption difference spectra for the bromide and chloride bound WT GtACR1 are depicted in **Figure 3.3.15**. The measurements were performed with pump pulse at 532 nm and recorded from 100 ns to 1 s. Global fitting of the difference spectra produced five lifetimes similar to the chloride bound form structure at the same pH 7.5, with two fast lifetimes, 672 ns and 5.6 μs, two slow lifetimes, 25 ms and 376 ms, and the lifetime of the minor component at 912 μs. Decomposition of the sequential intermediates produced four spectral forms, and obscured any additional intermediates. The time evolution of the spectral forms produced from the decomposition of the sequential intermediates for the chloride and bromide bound protein is shown in **Figure 3.3.16**. The time-dependent concentration

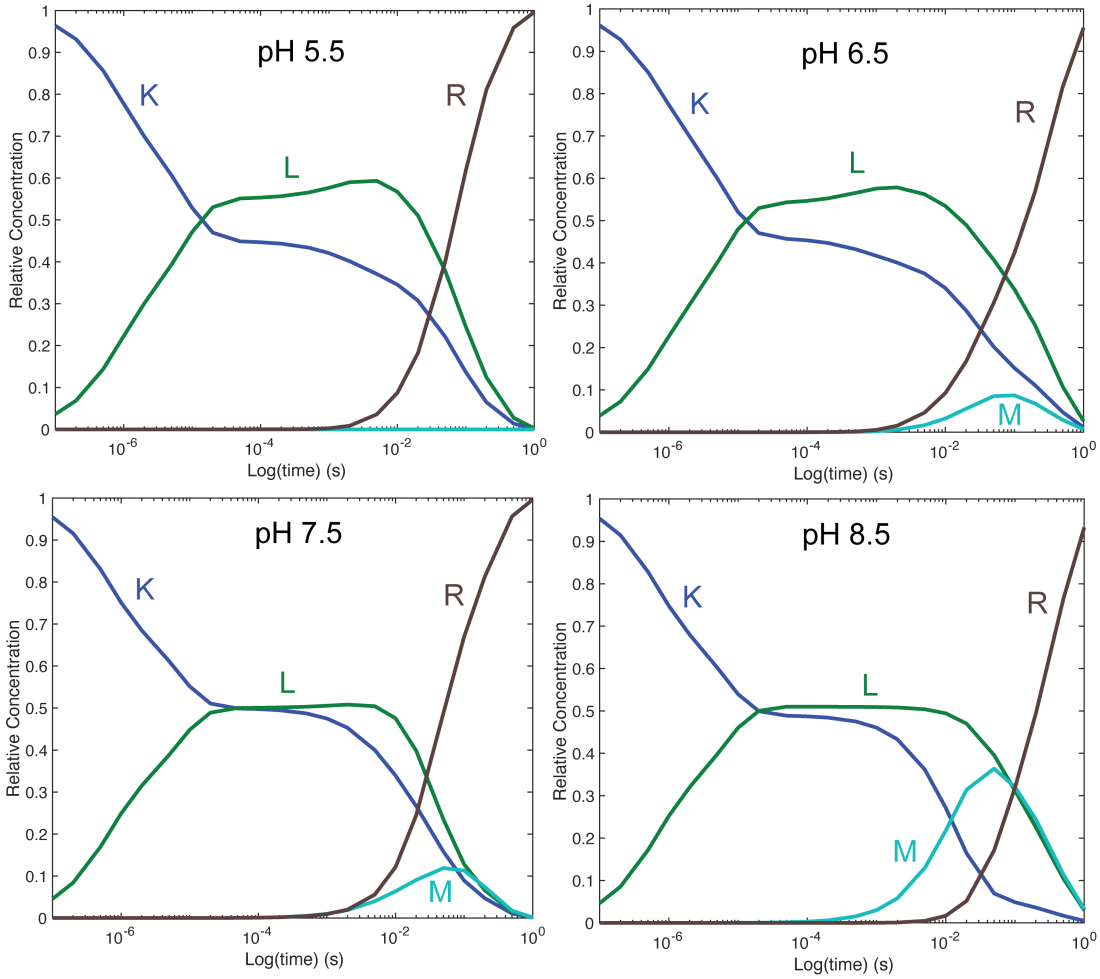

Figure 3.3.14: Time dependent concentration profile of the absolute intermediate spectra of WT GtACR1 in pH 5.5, 6.5, 7.5, and 8.5. Each sample was suspended in 20 mM HEPES with 300 mM NaCl, 5% glycerol, and 0.03% DDM. The pH was adjusted with NaOH and HCl.

curves display some explicit differences. There is a considerable larger amount of the L form relative to the K form for the bromide bound state. The bromide bound state also exhibits a smaller amount of the M form, as is apparent in **Figures 3.3.15 and 3.3.16**. The crystal structure of WT GtACR has a salt bridge between R94 and D234.[11] This salt bridge is important for the proton transfer pathway during the photochemical reaction.[29] The bromide bound protein structure has an alternative salt bridge between R94 and E223, which may explain the depletion of the M-intermediate in the time-resolved optical absorption spectra.[28]

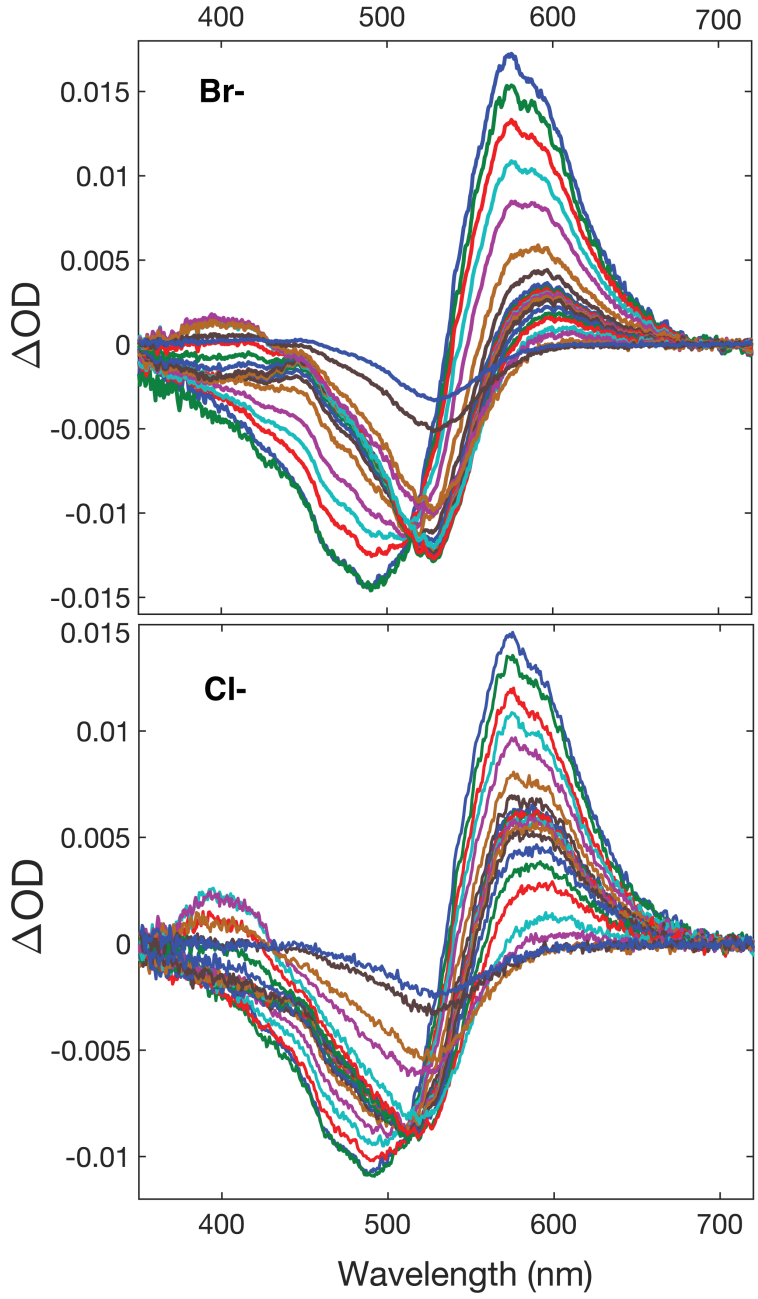

Figure 3.3.15: Time-resolved optical absorption spectra of the bromide bound, and chloride bound WT GtACR1. Each sample was suspended in 20 mM HEPES pH 7.5 with 5% glycerol, and 0.03% DDM. The buffer for the chloride bound protein contains 300mM NaCl and the buffer for the bromide bound protein contains 350 mM NaBr. The difference spectra were recorded at 22 logarithmically spaced time points from 100 ns to 1 s.

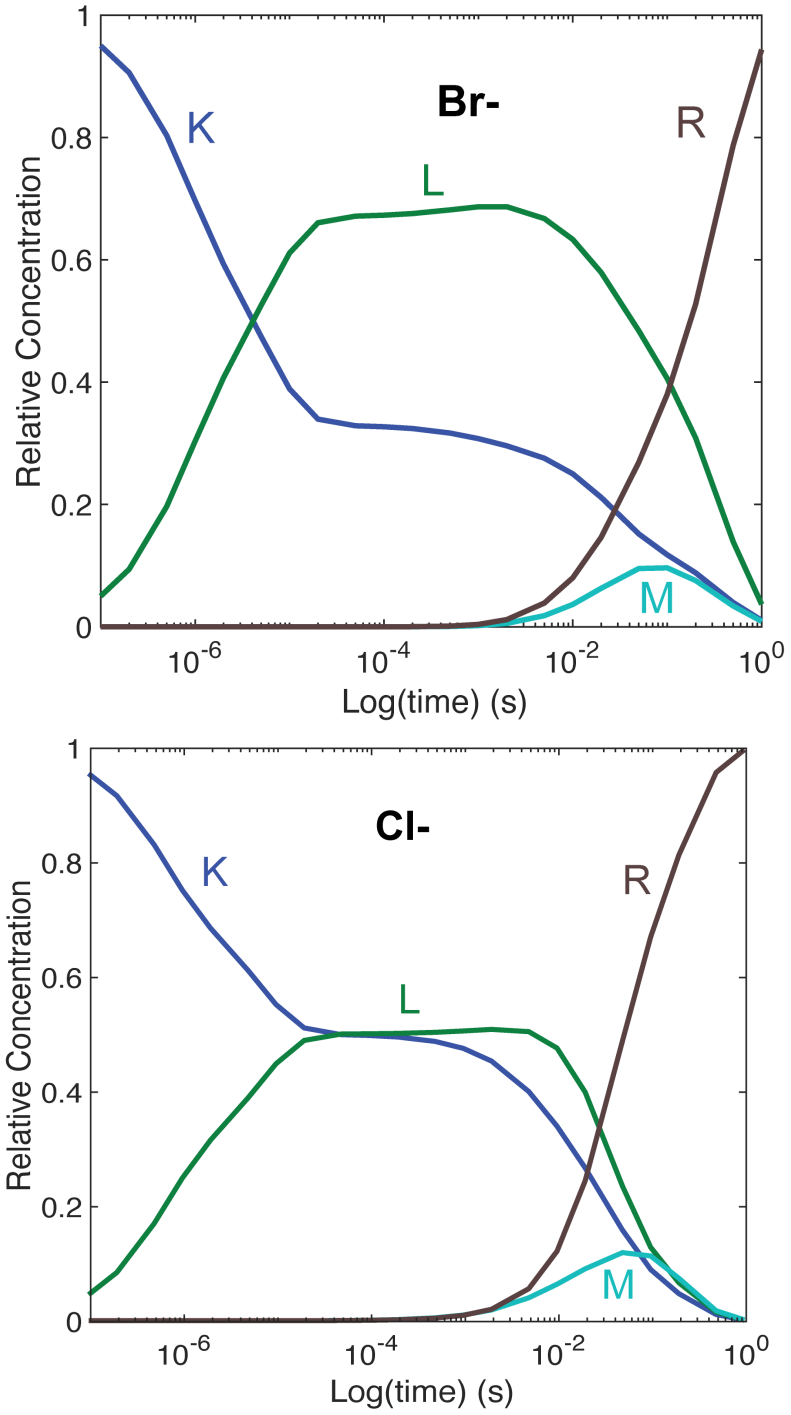

Figure 3.3.16: Time dependent concentration profiles of the spectral forms produced from the decomposition of the sequential intermediates for the bromide and chloride bound WT GtACR1.

3.4 Summary

Analysis of the WT GtACR time-resolved optical absorption data found a red-shifted K form and a blue-shifted L form that existed for the duration of the experiment. This observation is inconsistent with the previously published models that describe a reversible step between K and L, followed by an irreversible step for the decay of L.[16,27] The analysis of the WT TROD data strongly suggests the presence of isospectral intermediates in the photochemical reaction mechanism. It is not unusual for two spectral transitions with similar rates and forms to appear as one transition with an average lifetime. The presence of a K form and an L form for the length of the experiment could represent such a case. Changes to solution pH and anion substrate did not resolve any new intermediate spectral forms. Interestingly, a higher pH revealed a clear transition between the red-absorbing K form and the deprotonated M form. Previous models had only defined the formation of M from the decay of an L form.[16,27] Chapter 4 will investigate a handful of interesting mutants to resolve any additional intermediates and attain clues on the photochemical reaction mechanism of GtACR1.

3.5 References

1. Govorunova, E. G., Sineshchekov, O. A., Janz, R., Liu, X. & Spudich, J. L. Natural light-gated anion channels: A family of microbial rhodopsins for advanced optogenetics. *Science.* **349**, 647–650 (2015).
2. Sineshchekov, O. A. *et al.* Rhodopsin-mediated photoreception in cryptophyte flagellates. *Biophys. J.* **89**, 4310–4319 (2005).
3. Sineshchekov, O. A., Jung, K. H. & Spudich, J. L. Two rhodopsins mediate phototaxis to low- and high-intensity light in Chlamydomonas reinhardtii. *Proc. Natl. Acad. Sci. U. S. A.* **99**, 8689–8694 (2002).
4. Govorunova, E. G., Sineshchekov, O. A., Li, H. & Spudich, J. L. Microbial rhodopsins: Diversity, mechanisms, and optogenetic applications. *Annu. Rev. Biochem.* **86**, 845–872 (2017).
5. Govorunova, E. G. *et al.* The expanding family of natural anion channelrhodopsins reveals large variations in kinetics, conductance, and spectral sensitivity. *Sci. Rep.* **7**, (2017).
6. Lórenz-Fonfría, V. A. & Heberle, J. Channelrhodopsin unchained: Structure and mechanism of a light-gated cation channel. *Biochim. Biophys. Acta - Bioenerg.* **1837**, 626–642 (2014).
7. Mauss, A. S., Busch, C. & Borst, A. Optogenetic neuronal silencing in Drosophila during visual processing. *Sci. Rep.* **7**, (2017).
8. Messier, J. E., Chen, H., Cai, Z. L. & Xue, M. Targeting light-gated chloride channels to neuronal somatodendritic domain reduces their excitatory effect in

the axon. *Elife* **7**, 1–21 (2018).

9. Mohammad, F. *et al.* Optogenetic inhibition of behavior with anion channelrhodopsins. *Nat. Methods* **14**, 271–274 (2017).

10. Mahn, M., Prigge, M., Ron, S., Levy, R. & Yizhar, O. Biophysical constraints of optogenetic inhibition at presynaptic terminals. *Nat. Neurosci.* **19**, 554–556 (2016).

11. Li, H. *et al.* Crystal structure of a natural light-gated anion channelrhodopsin. *Elife* **8**, 1–21 (2019).

12. Kim, Y. S. *et al.* Crystal structure of the natural anion-conducting channelrhodopsin GtACR1. *Nature* **561**, 343–348 (2018).

13. Sineshchekov, O. A., Govorunova, E. G., Li, H. & Spudich, J. L. Gating mechanisms of a natural anion channelrhodopsin. *Proc. Natl. Acad. Sci.* **112**, 14236–14241 (2015).

14. Lanyi, J. K. Proton transfers in the bacteriorhodopsin photocycle. *Biochim. Biophys. Acta - Bioenerg.* **1757**, 1012–1018 (2006).

15. Lanyi, J. K. Bacteriorhodopsin. *New Compr. Biochem.* **23**, 75–101 (2004).

16. Sineshchekov, O. A., Li, H., Govorunova, E. G. & Spudich, J. L. Photochemical reaction cycle transitions during anion channelrhodopsin gating. *Proc. Natl. Acad. Sci.* **113**, E1993–E2000 (2016).

17. Yi, A., Mamaeva, N., Li, H., Spudich, J. L. & Rothschild, K. J. Resonance raman study of an anion channelrhodopsin: effects of mutations near the retinylidene Schiff base. *Biochemistry* **55**, 2371–2380 (2016).

18. Andersen, L. H. *et al.* Absorption of schiff-base retinal chromophores in vacuo. *J. Am. Chem. Soc.* **127**, 12347–12350 (2005).

19. Nakanishi, K., Balogh-Nair, V., Amaboldi, M., Tsujimoto, K. & Honig, B. An external point-charge model for bacteriorhodopsin to account for its purple color. *Journal of the American Chemical Society* vol. 102 7945–7947 (1980).

20. Mathies, R. & Stryer, L. Retinal has a highly dipolar vertically excited singlet state: Implications for vision. *Proc. Natl. Acad. Sci. U. S. A.* **73**, 2169–2173 (1976).

21. Schenkl, S., Van Mourik, F., Van Der Zwan, G., Haacke, S. & Chergui, M. Probing the ultrafast charge translocation of photoexcited retinal in bacteriorhodopsin. *Science.* **309**, 917–920 (2005).

22. Jäger, S. *et al.* Chromophore structural changes in rhodopsin from nanoseconds to microseconds following pigment photolysis. *Proc. Natl. Acad. Sci. U. S. A.* **94**, 8557–8562 (1997).

23. Szundi, I. *et al.* Platymonas subcordiformis channelrhodopsin-2 function: I. The photochemical reaction cycle. *J. Biol. Chem.* **290**, 16573–16584 (2015).

24. Sineshchekov, O. A., Govorunova, E. G., Wang, J., Li, H. & Spudich, J. L. Intramolecular proton transfer in channelrhodopsins. *Biophys. J.* **104**, 807–817 (2013).

25. Linford, G. J. Time-resolved xenon flash-lamp opacity measurements. *Appl. Opt.* **33**, 8333 (1994).

26. Szundi, I., Lewis, J. W. & Kliger, D. S. Deriving reaction mechanisms from

kinetic spectroscopy. Application to late rhodopsin intermediates. *Biophys. J.* **73**, 688–702 (1997).

27. Dreier, M. A. *et al.* Time-resolved spectroscopic and electrophysiological data reveal insights in the gating mechanism of anion channelrhodopsin. *Commun. Biol.* **4**, (2021).

28. Li, H. *et al.* The crystal structure of bromide-bound GtACR1 reveals a pre-activated state in the transmembrane anion tunnel. *Elife* **10**, 2020.12.31.424927 (2021).

29. Tsujimura, M., Kojima, K., Kawanishi, S., Sudo, Y. & Ishikita, H. Proton transfer pathway in anion channelrhodopsin-1. *Elife* **10**, 1–17 (2021).

CHAPTER 4

Elucidation of the Kinetics of the S97E, D234N, A75E Variants:

Time-Resolved Absorption Spectroscopic Studies

4.1 Introduction

The anion channelrhodopsin-1 from *Guillardia theta* (GtACR1) is a seven-transmembrane protein with a retinal-based chromophore. GtACR1 is capable of conducting anions across a membrane when activated with light. The ion conduction process is connected to an intricate rearrangement of the protein's hydrogen bond network. Regions in which this rearrangement of the H-bond network are of particular importance are the constriction sites along the conducting channel and the protonated Schiff base region.[1,2] For the well-known proton pump bacteriorhodopsin from *Halobacterium salinarum*, the protonated Schiff base is neutralized by a nearby (~5Å) aspartate (D85).[3] This conserved site on all so-far known anion channelrhodopsins is not charged and cannot neutralize the protonated Schiff base. For example, GtACR1 contains a serine at this position (S97). Mutation of this residue to a carboxylic group resulted in a near loss-of-function of channel activity.[4]

The aspartate residue (D234) in the protonated Schiff base region has been found to be both in a neutral state and a deprotonated state in the ground form.[1,4–6] Mutation from aspartate to arginine usually does not significantly alter protein function for neutral residues. Some results report D234N mutants as functional, while others report loss-of-function.[1,4] Recently, the aspartate residue (D234) in the protonated Schiff base region was confirmed to be deprotonated in the ground form of WT GtAC1, and has a direct H-bond interaction with the protonated Schiff base that is at a distance of 3.2Å.[6] This interaction is reasoned to neutralize the protonated Schiff base. It is hypothesized that the Schiff base retinal needs to be at least partially protonated to

maintain function, as it aids in shuttling Cl- across the membrane.[2] Loss-of-function is well-understood if D234 is deprotonated in the ground form, as a concurrent structural reorientation of a neighboring glutamate residue (E68) produces energetic barriers for ion conduction.[6]

An additional observation of the D234N variant was the formation of an earlier blue-shifted intermediate, the M-state. Mutations of residues that temporally shift the M intermediate may also perturb other intermediates and permit the resolution of isospectral intermediates. Another mutation known to perturb the M-intermediate is an alanine to glutamate mutation at A75. The A75 residue exists near the extracellular constriction sites along the conducting channel at a distance of > 9Å from the Schiff base, and an A75E mutation results in a bulkier charged functional group protruding into the channel.[7] Preliminary studies on the A75E mutant found a longer-lived M-intermediate, indicating a slower reprotonation of the Schiff base intermediate.[7] The purpose of this study is to parse out isospectral intermediates through studying mutations that perturb the electrostatics near the chromophore and H-bond network throughout the channel.

4.2 Materials and Methods

The materials and methods were outlined previously in Chapter 2. For S97E GtACR1 in pH 7.4 buffer, a total of 400 time-resolved optical absorption spectroscopic measurements were taken for each of the 22 delay times. For S97E in pH 5.6 buffer, 100 time-resolved optical measurements were made, and for S97E GtACR1 at pH 9, 380 time-resolved optical measurements were taken at the 22 delay times. These measurements were taken on nine separate days for two distinct samples. For both D234N GtACR1at pH 7.4 and 4.5, 100 measurements were taken on two separate days for one sample. For A75E in pH 7.4, 100 measurements were taken in one day on one sample. The total of measurements for each mutant at its respective pH was combined in a weighted average before the subsequent analysis.

4.3 Results and Discussion

4.3.1 S97E Mutant

Figure 4.3.1 shows the absorption spectra of WT GtACR1 and the S97E mutant. At neutral pH, the S97E mutant absorption is broadened and red-shifted. Unlike the wild-type, the S97E mutant ground state absorption was sensitive to pH (**Figure 4.3.2**). This was observed by other researchers, and a pK_a of 8 was reported.[4] The absorption spectrum of S97E near the pK_a is significantly broader than the spectra at pH 5.6 and 9.

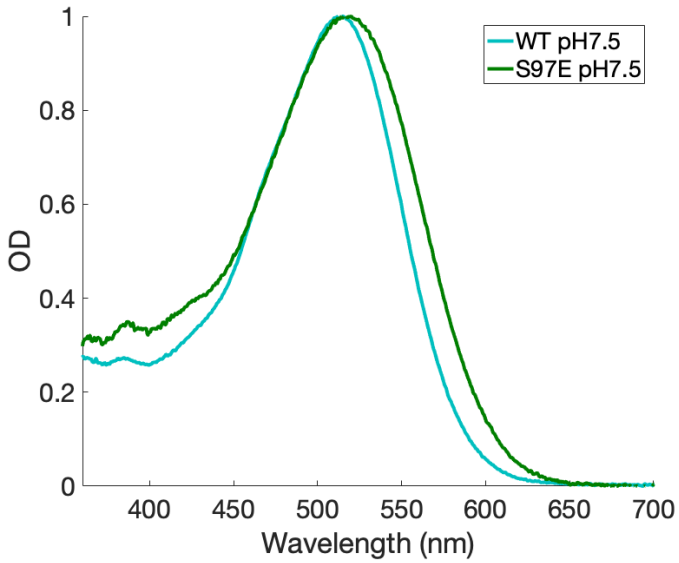

Figure 4.3.1 Absorption spectra of WT GtACR1 and S97E mutant normalized to the main band of the chromophore. The WT main band is at 515 nm. S97E mutant has a broader main band transition that occurs around 520 nm. Both samples are in 20mM HEPES pH 7.5 with 300 mM NaCl, 5% glycerol, and 0.03% DDM.

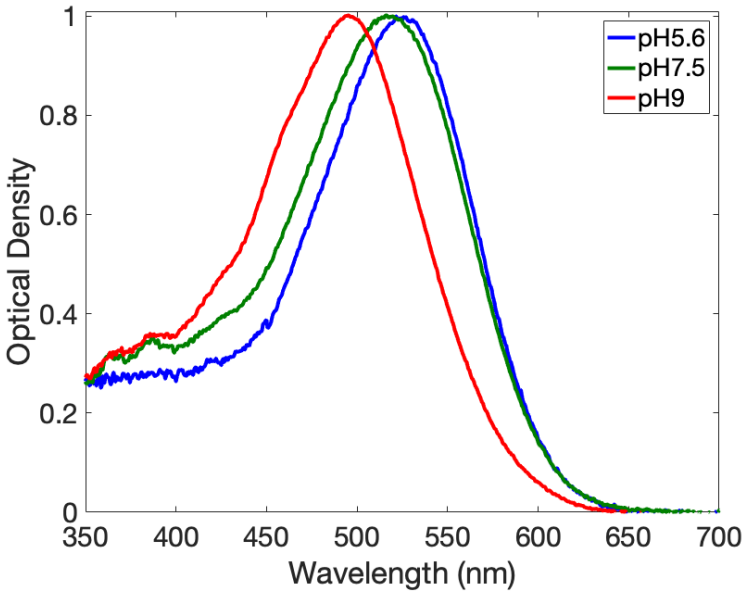

Figure 4.3.2: Absorption spectra of the S97E mutant in pH 5.6 (blue), 7.5 (green), and 9 (red). Each sample was suspended in 20 mM HEPES with 300 mM NaCl, 5% glycerol, and 0.03% DDM. pH was adjusted with NaOH and HCl.

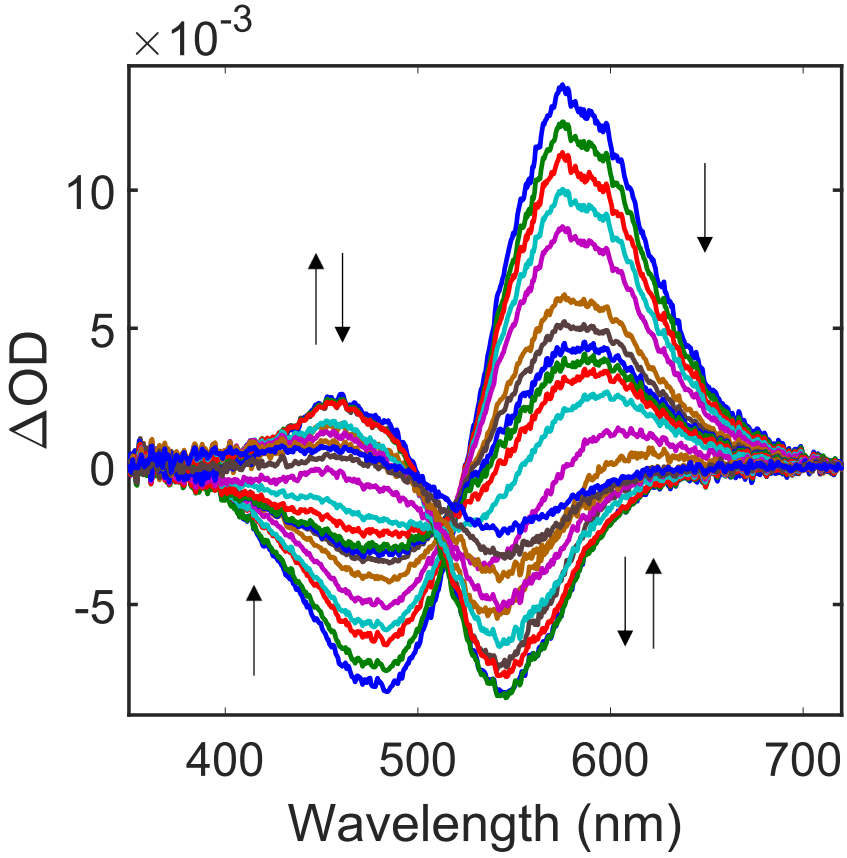

Figure 4.3.3: Time-resolved optical absorption difference spectra (post-minus pre-excitation) of the S97E mutant in 20 mM HEPES (pH 7.5) buffer with 300 mM NaCl, 5% glycerol, and 0.03% DDM. The difference spectra were recorded at 22 logarithmically spaced time points from 100 ns to 1 s. The first curve at 100 ns delay time has a prominent positive feature around 600 nm and a negative feature around 480 nm. The arrows describe the decay of these components from 100 ns to 100 μs. The formation of a positive blue-absorbing feature starts at 200 μs with a negative feature around 545 nm. These features grow in amplitude until 10 ms when they decay to the recovered form. The arrows describe the increase and then decrease in amplitude.

Time-resolved optical absorption difference spectra for S97E are shown in **Figure 4.3.3**. The difference spectra were recorded between 350 and 750 nm at logarithmically spaced time points between 100 ns and 1 s. The difference spectra of S97E contain a red-absorbing spectral form similar to the WT early in the experiment, as well as a similar blue-absorbing species later in the experiment. The S97E mutant exhibits two pronounced negative bands one at ~545 nm and the other ~480 nm, in contrast to the WT where only a single negative band corresponding to the recovered state at 515 nm was observed. The results from the SVD analysis are reported in **Figure 4.3.4**. SVD analysis resolved three **u**,**v**-vector pairs with significant values of 0.1986, 0.1433, and 0.0144 (**Figure 4.3.4 A**). The spectral components from the decomposition are shown in **Figure 4.3.4. B**. All three of the vectors have important spectral forms necessary for an adequate approximation. The time evolution of the spectral forms, the **v**-vectors, are presented in **Figure 4.3.4. C**. Exponential fitting of the **v**-vectors was performed with a series of 5 exponentials. Comparison of the **v**-vectors with the 5-exponential fit are presented in **Figure 4.3.5. A**, along with the residuals (**v**-vectors minus fit) in **Figure 4.3.5. B**. The 5-exponential fit was adequate as the temporal residuals are of the same magnitude as the random noise produced by the experiment. The apparent lifetimes produced from the fit were 319 ns, 4.84 μs, 439 μs, 59.1 ms, and 591 ms. **Figure 4.3.6 A** shows the spectral changes at each apparent lifetime. The first three ***b***-spectra (blue, green, and red, respectively) describe a transition from a red-absorbing spectral form to a blue-absorbing species. The other three ***b***-spectra show a blue-absorbing spectral form decaying into a red-absorbing species.

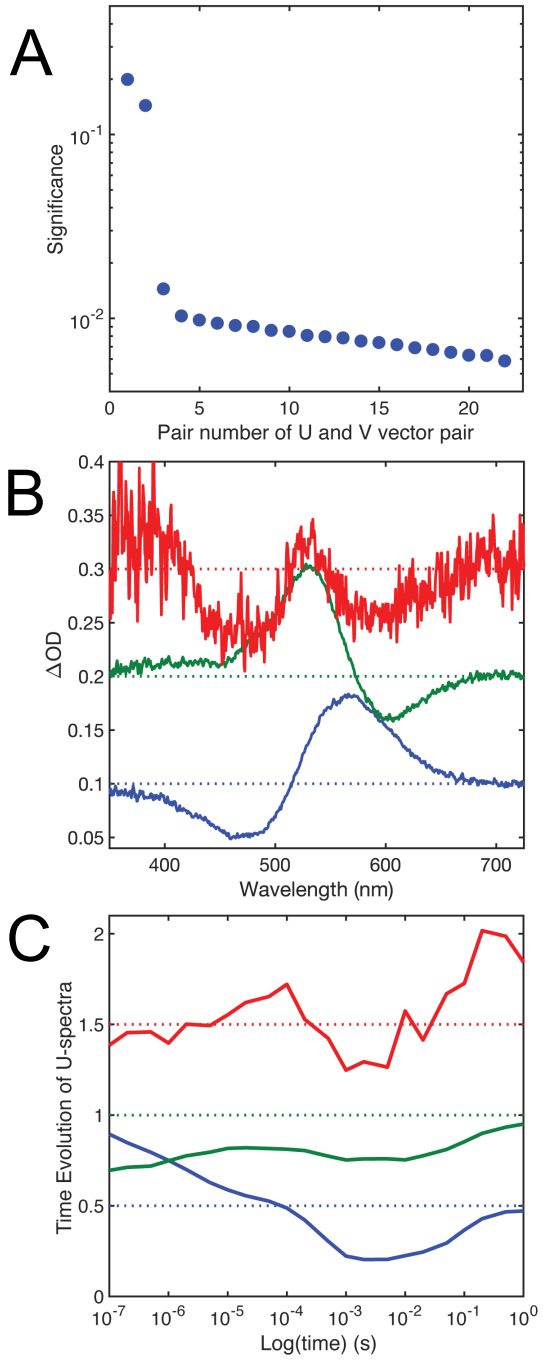

Figure 4.3.4: (A) Significance values of each **u**,**v**-vector pair for the S97E mutant. The first four **u**,**v**-vector pairs had significant values of 0.1986, 0.1433, and 0.0144, respectively. **(B)** Orthonormal basis spectra (**u**-spectra). **(C)** The time evolution of the **u**-spectra, called the **v**-vectors.

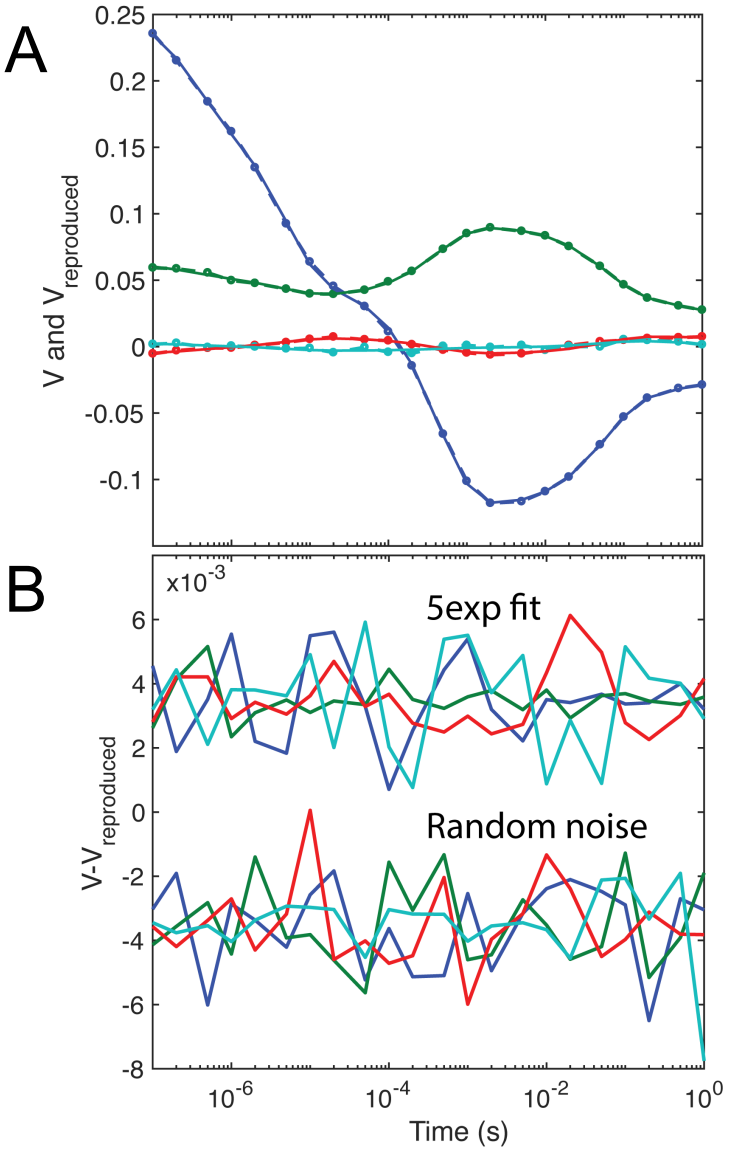

Figure 4.3.5: (A) The significant **v**-vectors for the S97E mutant determined from the SVD of the difference spectra (dots) compared to the reproduced vectors of the 5-exponential fit (solid lines). **(B)** The temporal residuals (data minus fit) for the five-exponential fit contrasted with the level of random noise produced from the experiment.

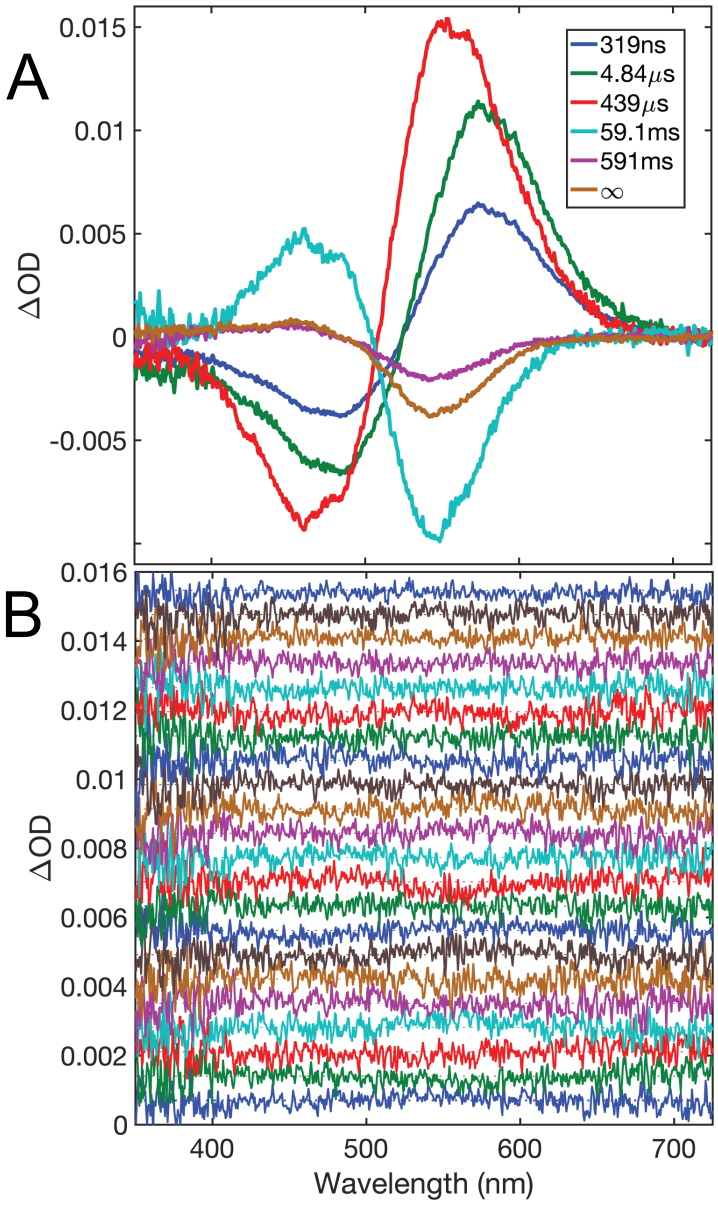

Figure 4.3.6: (A) The spectral changes, ***b***-spectra, for each apparent lifetime from the five-exponential fit of the time-resolved optical absorption data of the S97E mutant. The apparent lifetimes are presented in the legend. **(B)** The spectral residuals of the fit are compared to the data for each delay time (increasing from bottom to top from nanoseconds to seconds).

Figure 4.3.7 shows the intermediate difference spectra using a proposed sequential scheme for the 5-exponential fit. A red-absorbing component persists throughout most of the experiment as is observed in the first three intermediates. There is also a significant blue absorbing species in Int4 that does not coincide with the deprotonated state. Decomposing the sequential intermediates resolved five classes of unique spectral forms. **Table 4.1** lists the fractional composition of each spectral form within the sequential intermediates. **Figure 4.3.8** presents the product of the decomposition of the sequential intermediates, and **Figure 4.3.9 A** shows the four unique spectral forms resolved for the S97E mutant. As with the WT, a red-absorbing class centers around 540 nm. Strikingly, the S97E mutant reveals a new class of spectral forms around 480 nm. This new spectral form appears to be similar to the L form for the WT. However, it cannot be the L form because it appears later in the experiment (**Figure 4.3.9 B**). The L form is reserved as the first species to appear from the decay of the K form. For the S97E mutant, the L form is isospectral to the recovered state. S97E also showed significantly less amount of the M-form which corresponds to the deprotonated Schiff base. The pK_a of this residue was found to be ~8.[1] Experiments at higher pH in this work resulted in degradation of the protein, especially in combination with the laser stimulus. This demonstrated that when the residue has the ability to become involved with the proton transfer pathway, the protein is destroyed, perhaps due to hydrolyzation with water or repulsions with the anion conduction pathway near the Schiff base. **Figure 4.3.9 B** show the temporal evolution of the unique spectral forms.

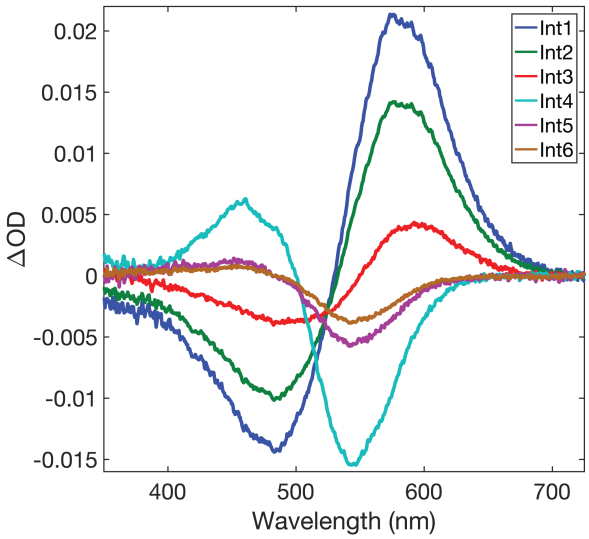

Figure 4.3.7: Difference spectra of the intermediates of the S97E mutant assuming a sequential scheme for the 5-exponential fit.

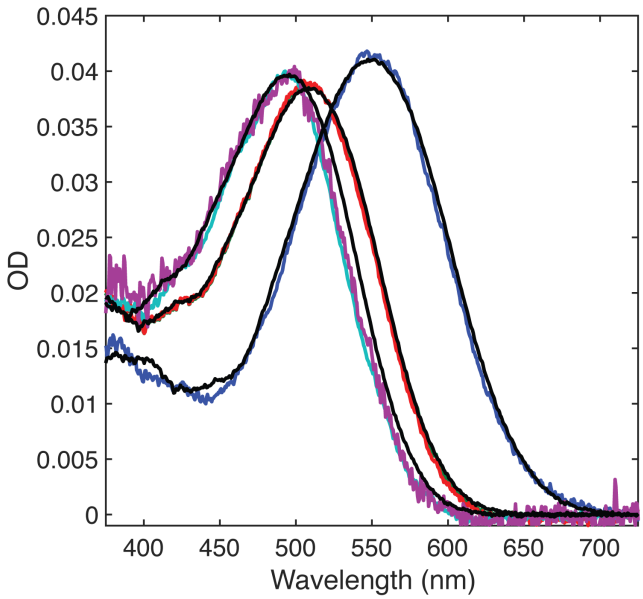

Figure 4.3.8: Unique spectral forms from the decomposition of the sequential intermediates for the S97E mutant. The black curves are both the same bleach spectrum wavelength shifted to overlay the decomposed intermediates. The blue curve is the first red-shifted spectral form. The green, red, magenta, and cyan curves are derived from the second, third, fourth, and fifth sequential intermediates, respectively. The recovered and M forms are not shown.

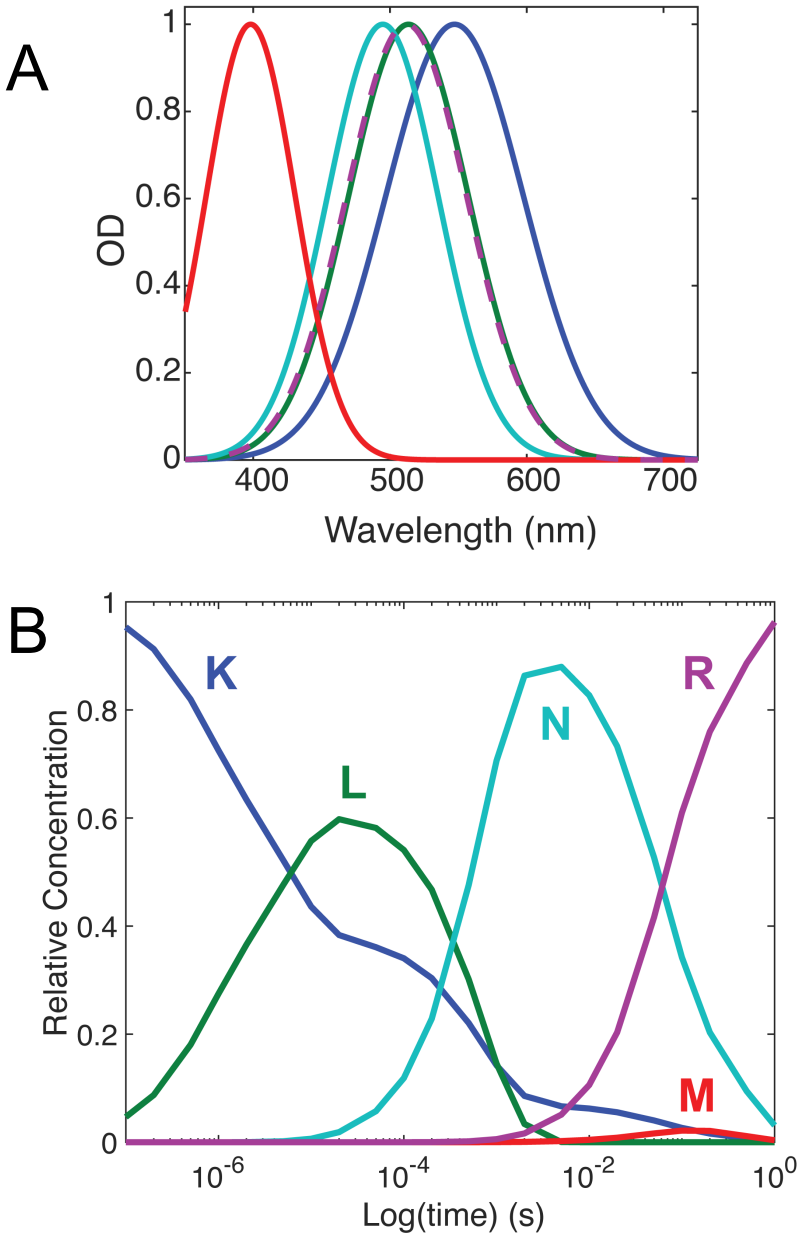

Figure 4.3.9: (A) Absolute intermediate spectral forms determined from decomposing the sequential intermediates of the S97E mutant. This includes K (blue, line), L (green, line), M (red, line), R, (magenta, dashed) A new distinct spectral form was resolved that is isospectral to the recovered state, N (cyan, line). **(B)** Time dependent concentration profile of the absolute intermediate spectral forms for the S97E mutant.

S97E	SeqInt1	SeqInt2	SeqInt3	SeqInt4	SeqInt5	SeqInt6
K	1	0.72	0.32	0.07	0.01	0
L	0	0.28	0.68	0	0	0
M	0	0	0	0	0.013	0
N	0	0	0	0.93	0.127	0
R	0	0	0	0	0.85	1

Table 4.1: Fractional composition of the spectral forms, K, L, M, N, and R within the intermediates from the sequential scheme of the S97E mutant.

4.3.2 D234N Mutant

Figure 4.3.10 is the dark form absorption spectra of the dark forms of the WT and D234N mutant. The spectra are nearly identical in spite of the wavelength at the maximum absorption differing by 3nm. **Figure 4.3.11** shows the time-resolved optical absorption difference spectra of the D234N mutant recorded between 350 to 750 nm at 22 logarithmically space time points from 100 ns to 1 s. Similar to the WT, the D234N mutant has an early red-shifted spectral component that persists for most of the experiment. The D234N mutant does not show as much of the blue-shifted spectral M-like component as the wild-type.

Figure 4.3.12 is the results of the SVD analysis on the D234N mutant. Four **u**,**v**-vector pairs were produced from the SVD of the D234N mutant with significant values of 0.2180, 0.1225, 0.0200, and 0.0100, respectively (**Figure 4.3.12 A**). The spectral components from the SVD are in **Figure 4.3.12 B**. The fourth **u**-vector maintains a minor spectral shape that is necessary for a good approximation to the raw data. The time evolution of the spectral forms is depicted in **Figure 4.3.12 C**.

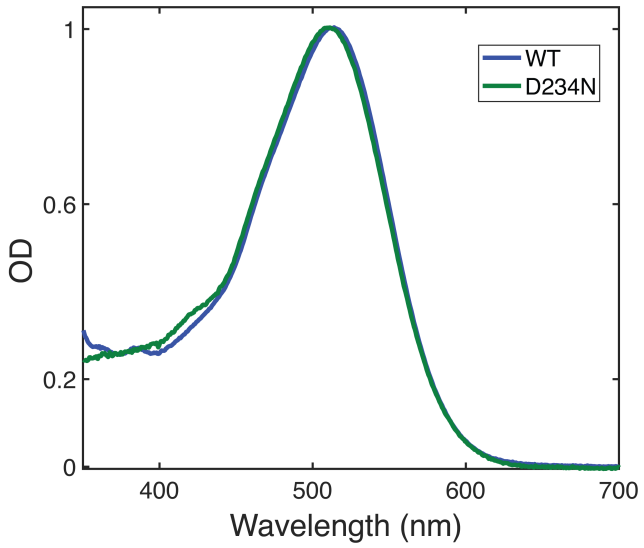

Figure 4.3.10: Absorption spectrum of the dark form of WT GtACR1 and D234N mutant in 20 mM HEPES (pH 7.5) buffer with 300 mM NaCl, 5% glycerol, and 0.03% DDM.

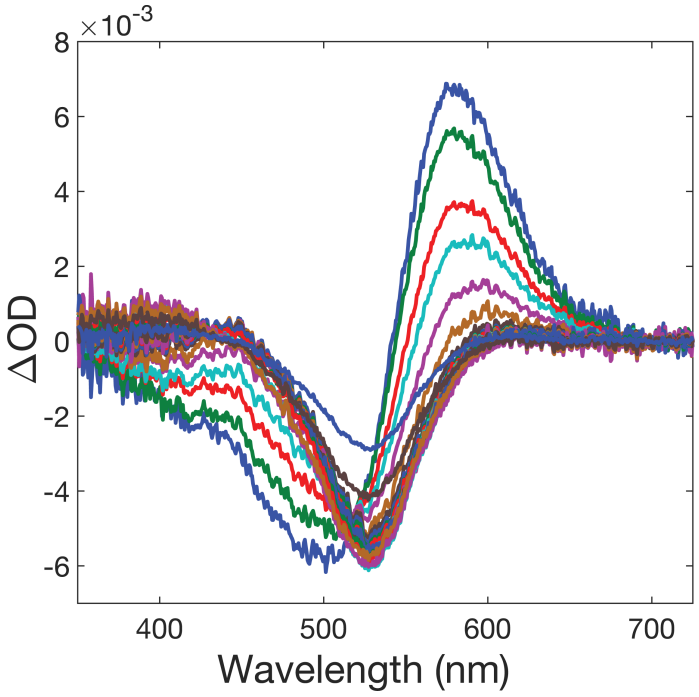

Figure 4.3.11: Time-resolved optical absorption difference spectra (post- minus pre-excitation) of the D234N mutant in 20 mM HEPES (pH 7.5) buffer with 300mM NaCl, 5% glycerol, and 0.03% DDM. The difference spectra were recorded at 22 logarithmically spaced time points from 100 ns to 1 s.

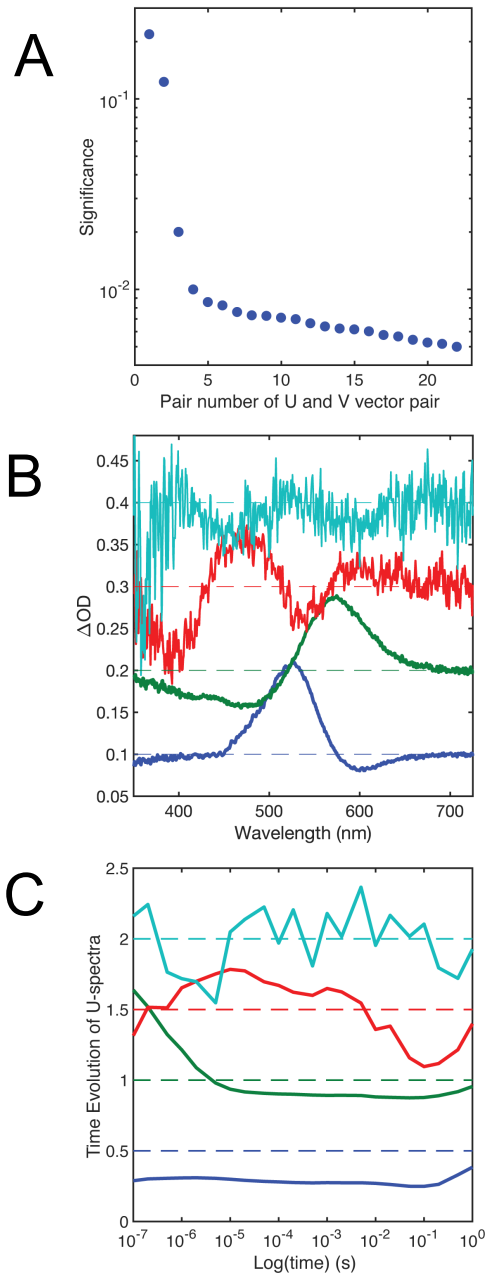

Figure 4.3.12.: (A) Significance values of each **u**,**v**-vector pair for the D234N mutant. The first four **u**,**v**-vector pairs are much more significant with values of 0.2180, 0.1225, 0.0200, and 0.0100, respectively. (**B)** Orthonormal basis spectra (**u**-spectra). (**C)** The time evolution of the **u**-spectra, called the **v**-vectors.

Exponential fitting of the time evolution of the **u**-spectra of the D234N mutant was performed with 5-exponentials. The 5-exponential fit overlaying the **v**-vectors is depicted in **Figure 4.3.13 A.** The residuals for the 5-exponential fit compared with the noise produced in the experiment show an adequate fit (**Figure 4.3.13 B**). The apparent lifetimes produced from the 5-exponential fit were 214 ns, 1.69 μs, 16.1μs, 36.5 ms, and 814 ms. The spectral changes, ***b***-spectra, at each apparent lifetime for the 5-exponential fit are presented in **Figure 4.3.14 A**. Similar to the WT, the first two ***b***-spectra (blue and green, respectively) for the D234N mutant show a decay of the red-shifted K-like form to an L-like form. The red and cyan curves in **Figure 4.3.14 A** reveal both the K-like and L-like forms decaying and an M-like form appearing. The magenta curve exhibits an M-like form decaying into the recovered state. Along with the temporal residuals in **Figure 4.3.13 B,** the spectral residuals shown in **Figure 4.3.14 B** affirm the goodness of the fit.

Figure 4.3.15 shows the spectra of the 6 intermediates for the D234N mutant assuming a sequential scheme for the 5-exponential fit. The first and second intermediates (blue and green, respectively) contain a significant portion of the red-shifted species. The blue-shifted, deprotonated species appears later than in the WT sequential intermediates, showing up in the second to last intermediate (magenta). **Figure 4.3.16** shows the decomposition of the sequential intermediates into unique absolute spectral forms of the D234N mutant. The thick black curves are both the same bleach spectrum with the visible band wavelength shifted to overlay the decomposed

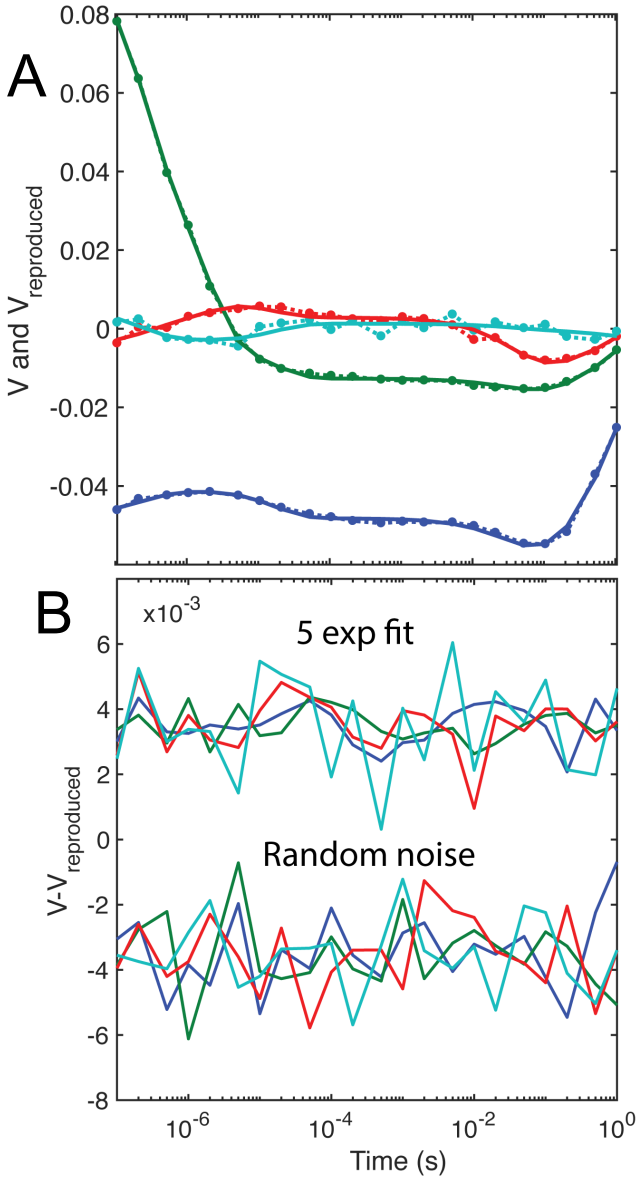

Figure 4.3.13: **(A)** Time evolution of the **u**-spectra (dotted lines) with the 5-exponential fit (solid lines) for the D234N mutant. **(B)** The temporal residuals (data minus fit) for the 5-exponential fit together with the level of random noise produced from the experiment.

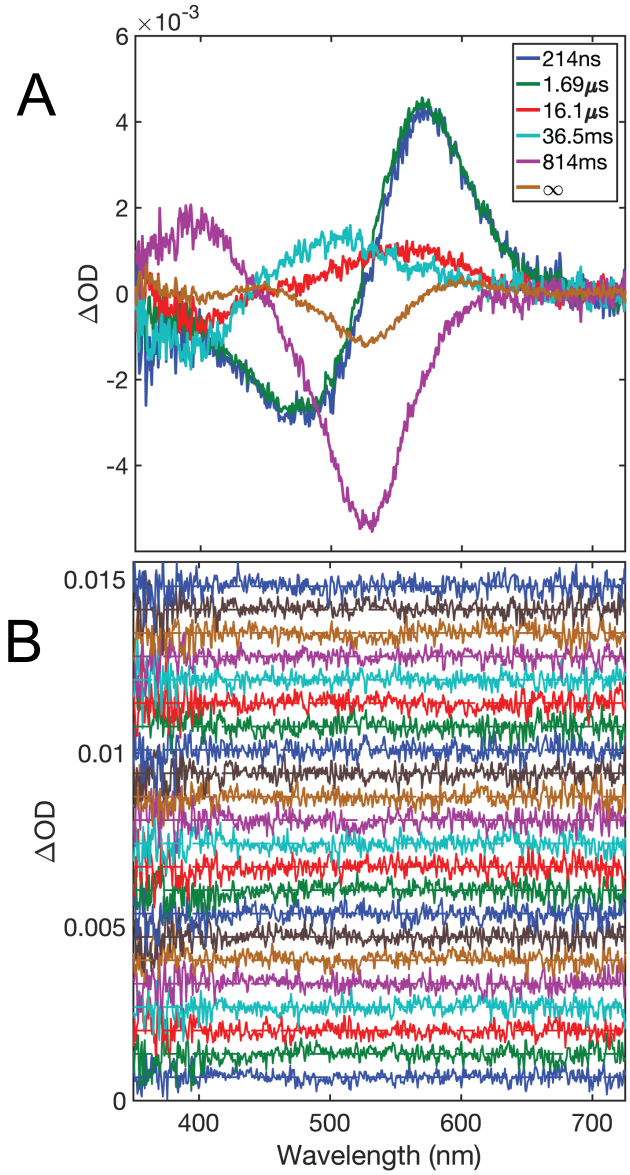

Figure 4.3.14: **(A)** The spectral changes, ***b***-spectra, for each apparent lifetime from the five-exponential fit of the time-resolved optical absorption data of the D234N mutant. The apparent lifetimes are presented in the legend. **(B)** The spectral residuals of the fit compared to the data for each delay time (increasing from bottom to top from nanoseconds to seconds).

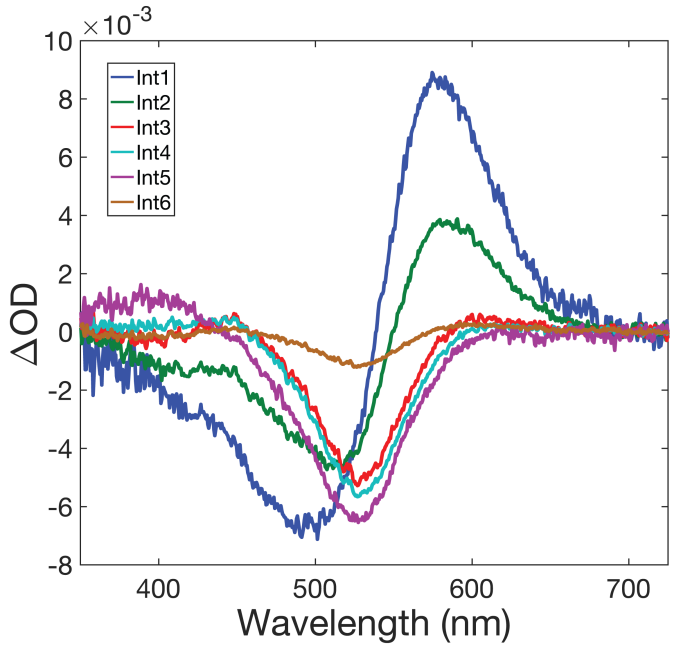

Figure 4.3.15: Difference spectra of the 6 intermediates of the D234N mutant from the sequential scheme.

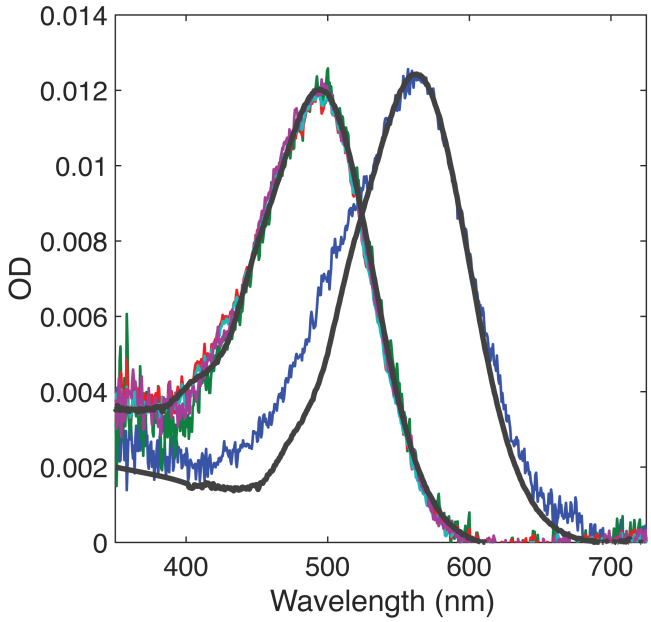

Figure 4.3.16: Unique spectral forms from the decomposition of the sequential intermediates. The black curves are both the same bleach spectrum wavelength shifted to overlay the decomposed intermediates. The blue curve is the first, red-shifted intermediate for the D234N mutant. The green, red, magenta, and cyan curves are the second, third, fourth, and fifth intermediates, respectively. The M form and recovered state are not shown

D234N	SeqInt1	SeqInt2	SeqInt3	SeqInt4	SeqInt5	SeqInt6
K	1	0.54	0.18	0.11	0.07	0
L	0	0.46	0.82	0.83	0.75	0
M	0	0	0	0.06	0.18	0
R	0	0	0	0	0	1

Table 4.2: Fractional composition of the spectral forms, K, L, M, and R within the sequential intermediates of D234N.

forms. Again, the red-shifted K-like form is present in all of the sequential intermediates. After subtracting this form in varying amounts, intermediates 2 through 4 (green, red, cyan, respectively) all had the same shape. The fifth sequential intermediate was composed of both the red-shifted K and the deprotonated blue-shifted forms. After the appropriate subtraction, had the same shape as intermediates 2 through 4. The decomposition resulted in the same unique spectral forms as the WT (K, L, M, and R). **Table 4.2** details the fractional contribution of each spectral form contained in the sequential intermediates. The unique absolute spectral forms for the D234N mutant are in **Figure 4.3.17 A**. The time evolution of the unique spectral forms is shown in **Figure 4.3.17 B**. The K and L forms for the D234N mutant appear to exist for the length of the experiment similar to the WT. However, much less of the K spectral form appears in this mutant. Unlike the WT, the M form in the D234N mutant appears early in the experiment and is present for a significantly longer time.

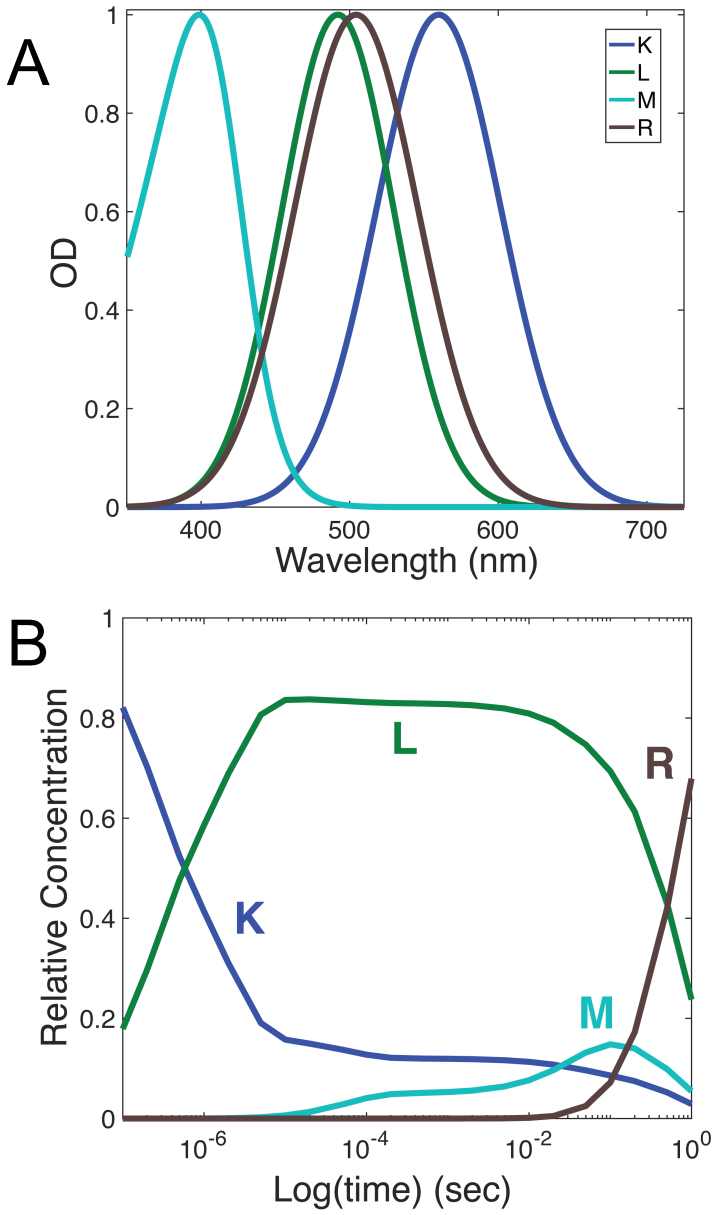

Figure 4.3.17: (A) Absolute intermediate spectra of the D234N mutant determined from decomposing the sequential intermediates into distinct spectra with similar shapes on the energy (wavenumber) scale. **(B)** Time dependent concentration profile of the absolute intermediate spectra for the D234N mutant.

4.3.3 A75E mutant

The absorption spectra of WT GtACR1 and the A75E mutant are shown in **Figure 4.3.18**. The wavelength of the maximum absorption for A75E is 511 nm, a 4 nm difference from the WT. The A75E mutant displayed a small shoulder at 425 nm. This is hypothesized to be a minor population of partially unfolded protein, as partially unfolded microbial rhodopsins have been reported to absorb around ~430 nm.[4] This species is not expected to affect the time-resolved absorption experiments as the laser at 532 nm will only excite the main band of the folded protein.

Figure 4.3.19 shows the time-resolved absorption difference spectra for the A75E mutant. The experiment was performed at 23 logarithmically spaced lifetimes from 100 ns to 2 s. The A75E mutant appears to have a longer lifetime with the last curve at 2 s exhibiting a significant amount of negative signal. The A75E mutant has a considerable amount of the red absorbing spectral form for the duration of the experiment, in line with the other GtACR1 variants. Similar to the D234N mutant, the A75E mutant does not appear to have as much of the blue-shifted, deprotonated intermediate.

SVD analysis on the time-resolved absorption difference spectra of the A75E mutant established four significant **u**,**v**-vector pairs. The significance values (**Figure 4.3.20 A**) for the four vector pairs were 0.3075, 0.1874, 0.0444, and 0.0097, respectively. The spectral components, **u**-spectra, from the decomposition are shown in **Figure 4.3.20B**. Although much less significant, the fourth **u**-vector has important spectral features necessary for an accurate approximation. The temporal components from the decomposition are displayed in **Figure 4.3.20C**.

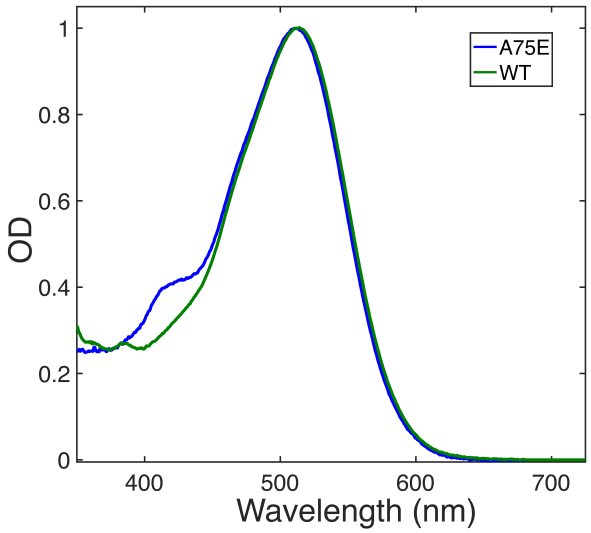

Figure 4.3.18: Absorption spectra of the dark form of WT GtACR1 and A75E mutant in 20 mM HEPES (pH 7.5) buffer with 300 mM NaCl, 5% glycerol, and 0.03% DDM.

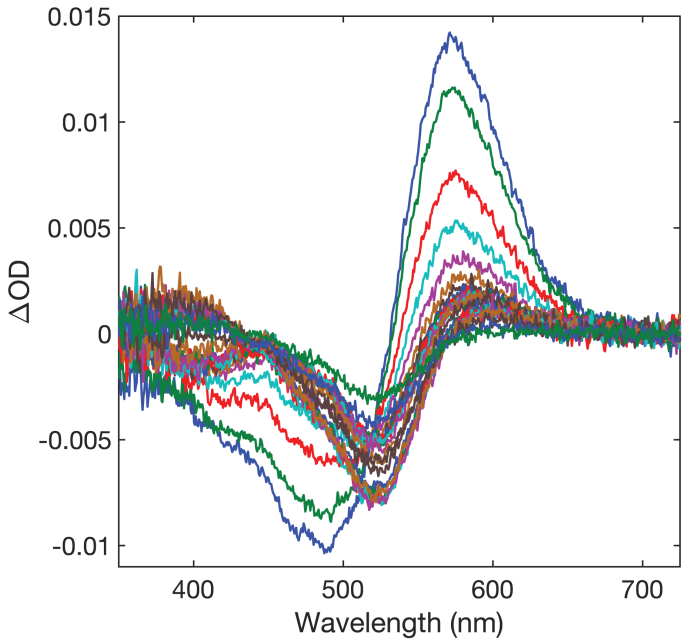

Figure 4.3.19: Time-resolved optical absorption difference spectra of the A75E mutant in 20 mM HEPES (pH 7.5) buffer with 300 mM NaCl, 5% glycerol, and 0.03% DDM. The difference spectra were recorded at 23 logarithmically spaced time points from 100 ns to 2 s.

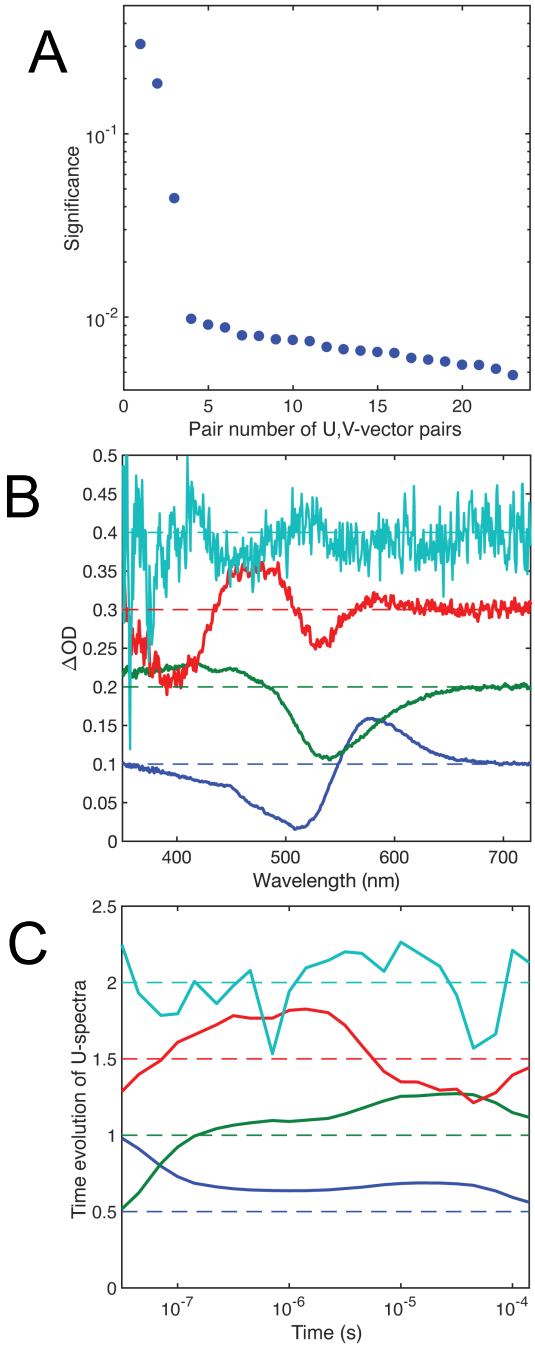

Figure 4.3.20: (A) Significance values of each **u**,**v**-vector pair for the A75E mutant. The first four **u**,**v**-vector pairs had significant values of 0.3075, 0.1874, 0.0444, and 0.0097, respectively. **(B)** Orthonormal basis spectra (**u**-spectra). (**C**) The time evolution of the **u**-spectra, called the **v**-vectors.

Figure 4.3.21 shows the exponential fitting of the **v**-vectors from the SVD of the time-resolved data for the A75E mutant. The **v**-vectors were fit with a series of 5, and 6-exponentials. **Figure 4.3.21 A** displays the **v**-vectors with the exponential fits, and **Figure 4.3.21 B** represents the temporal residuals from the fits. The 5-exponential fit exhibited a wave-like, non-random noise structure in the residuals in the hundreds of microsecond region. This region is of importance as it corresponds to the timing of the open channel state. The 6-exponential fit produced satisfactory residuals. The 6 apparent lifetimes resolved from the exponential fit were 363 ns, 3.73 μs, 140 μs, 2.60 ms, 162 ms, and 556 ms. The spectral changes associated with each apparent lifetime are shown in **Figure 4.3.22 A**. Similar to the other variants, the first two ***b***-spectra express a transition from a K-like form to L-like spectral form. However, the second ***b***-spectrum for the A75E mutant has a much smaller amplitude for the decay of the K-like spectral form than the other variants. A minor component appearing at 140 μs describes (when zoomed in) a transition from a K-like to L-like species. The ***b***-spectra with lifetimes of 2.60 ms and 162 ms both exhibit a transition from both K-like and L-like spectral forms to the blue-absorbing spectral form. The ***b***-spectrum associated with a lifetime at 556ms shows a transition from the blue-absorbing M-like form to the recovered state. The spectral residuals (data minus fit) for the 6-exponential fit displayed in Figure **5.3.22 B** confirm a good fit.

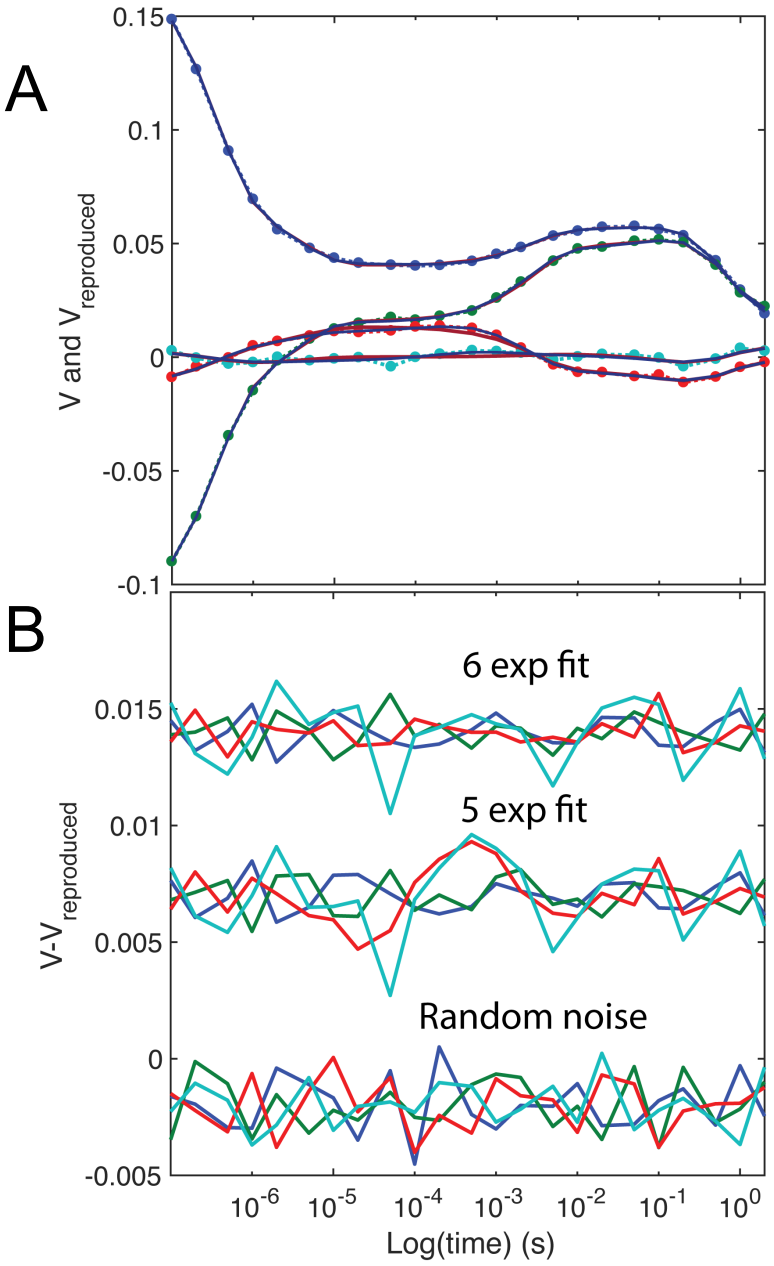

Figure 4.3.21: (A) The significant **v**-vectors of the A75E mutant determined from the SVD of the difference spectra (dots) compared to the reproduced vectors of the 5-exponential fit (solid red lines), 6-exponential fit (solid blue lines). **(B)** The temporal residuals (data minus fit) for the fits contrasted with the level of random noise produced from the experiment.

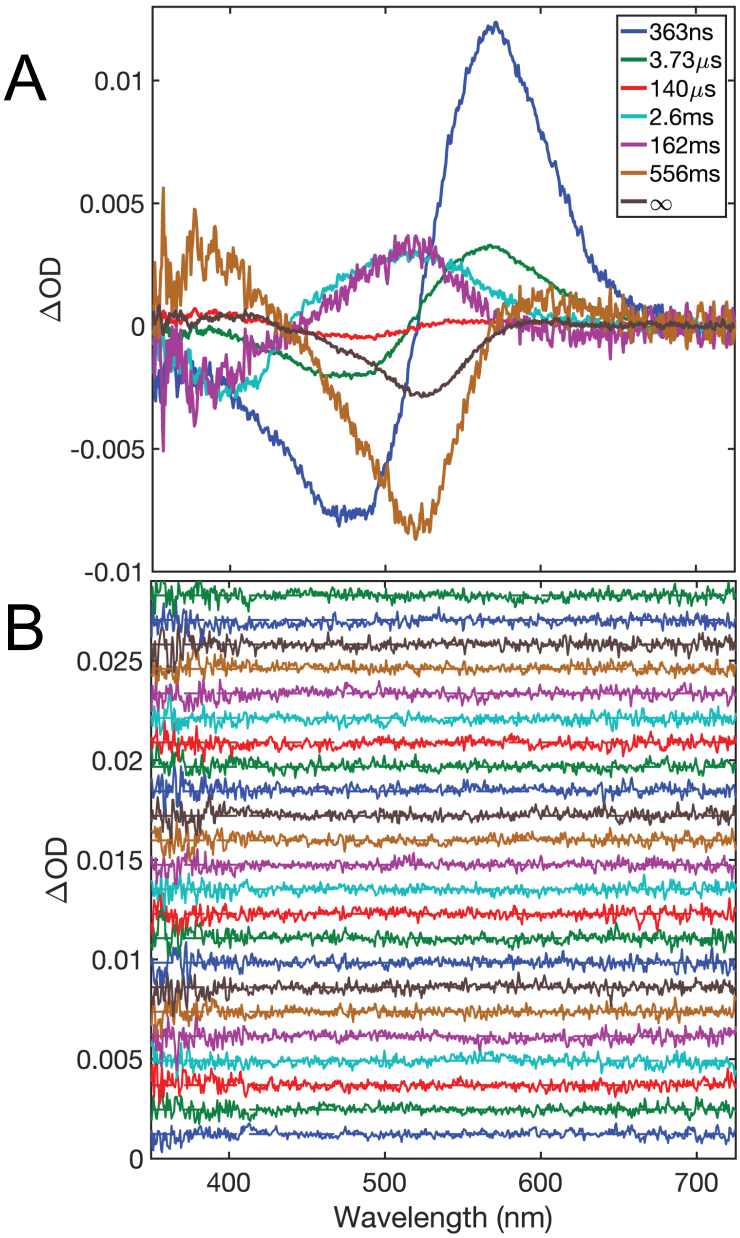

Figure 4.3.22: (A) The ***b***-spectra, for the 6-exponential fit. **(B)** The spectral residuals for the 6-exponential fit for each delay time (increasing from bottom to top from 100 nanoseconds to 2 seconds).

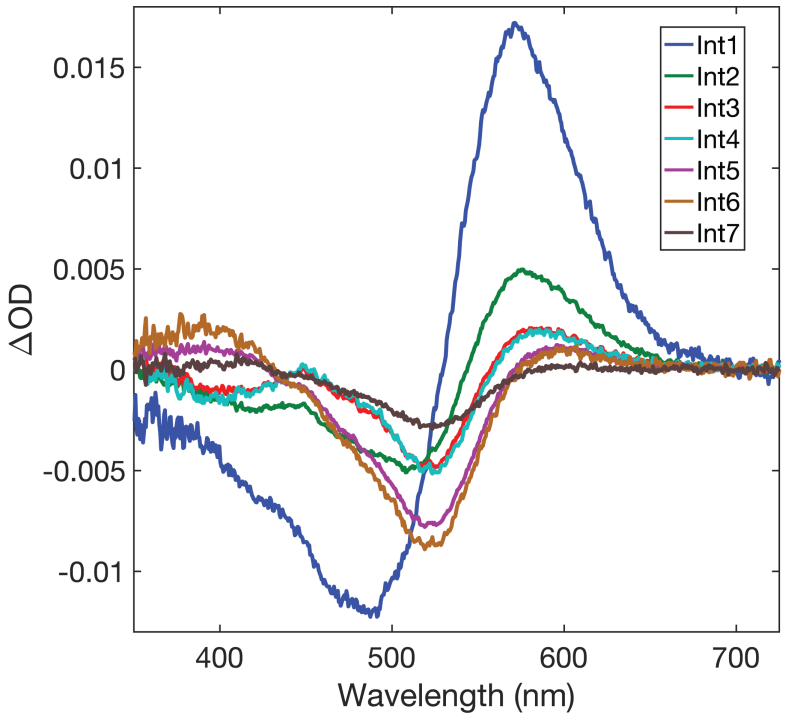

Figure 4.3.23: Difference spectra of the intermediates fpr the A75E mutant assuming a sequential scheme for the 6-exponential fit.

Assuming a sequential scheme for the 6-exponential fit for the A75E mutant produced the intermediate difference spectra in **Figure 4.3.23**. The first intermediate (blue) contains a significant portion of the red-shifted species, similar to the other variants. The second intermediate, green, contains the red-shifted intermediate, but to a lesser extent than the other variants. The blue-shifted, deprotonated species appears around the same time as in the WT, showing up in the third to last intermediate (magenta).

Figure 4.3.24 displays the results from the decomposition of the sequential intermediates. The black curves are the same bleach spectrum, wavelength shifted to

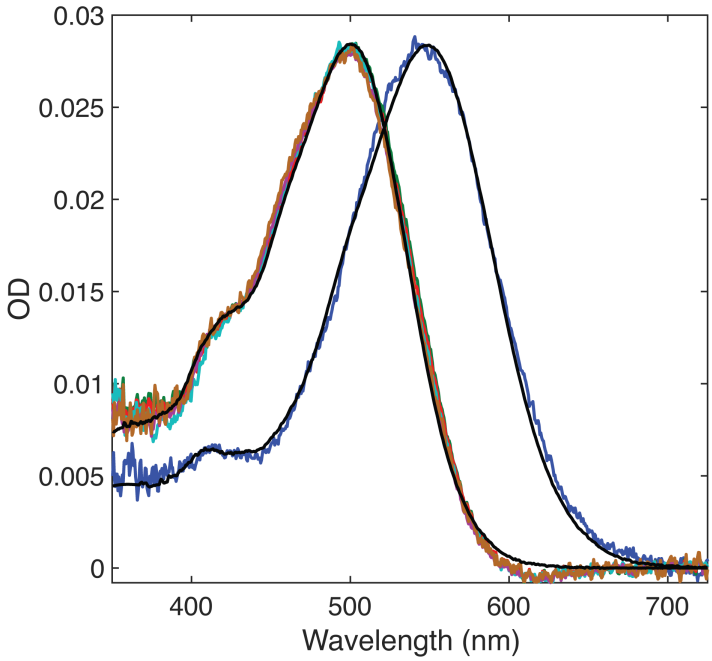

Figure 4.3.24: Decomposed spectral forms from the sequential intermediates. The black curves are both the same bleach spectrum wavelength shifted to overlay the decomposed spectral forms. The blue curve is the first, red-shifted spectral form. The green, red, magenta, cyan, and mustard curves are the second, third, fourth, fifth, and sixth intermediates, respectively. The M form and recovered state are not shown.

overlay the products of the decomposition. The blue curve is the first, red-shifted intermediate after the addition of the bleach. The green, red, magenta, cyan, and mustard curves are the second, third, fourth, fifth, sixth, and seventh intermediates, respectively. As with the other variants, all but the last recovered intermediate contains the red-shifted spectral form. After the subtraction of the red-shifted form and subsequent addition of the bleach, intermediates 2 through 4 were superimposable. Subtraction of the red-shifted and blue-shifted spectral forms was required for intermediates 5 and 6 to overlay. Decomposition of the A75E sequential intermediates yielded 4 distinct intermediate spectral forms. **Table 4.3** characterizes the amount of

A75E	SeqInt1	SeqInt2	SeqInt3	SeqInt4	SeqInt5	SeqInt6	SeqInt7
K	1	0.39	0.25	0.24	0.21	0.19	0
L	0	0.61	0.75	0.76	0.69	0.68	0
M	0	0	0	0	0.1	0.13	0
R	0	0	0	0	0	0	1

Table 4.3: Composition of the sequential intermediates of A75E in terms of spectral forms.

each spectral form in the sequential intermediates. **Figure 4.3.25 A** shows the absolute intermediate spectral forms resulting from the decomposition. Analogous to the WT and D234N mutant, A75E displayed K, L, M, and R during the photoreaction. **Figure 4.3.25 B** shows the time evolution of the absolute intermediates. Similar to the D234N mutant, the K form decays much more rapidly in the A75E mutant than in the WT. However, a significantly larger concentration of the red-absorbing spectral form occurs in the A75E mutant than the D234N mutant. The recovered form R appears much later than for the WT, which agrees with the longer lifetime of the on-state observed in electrophysiology.

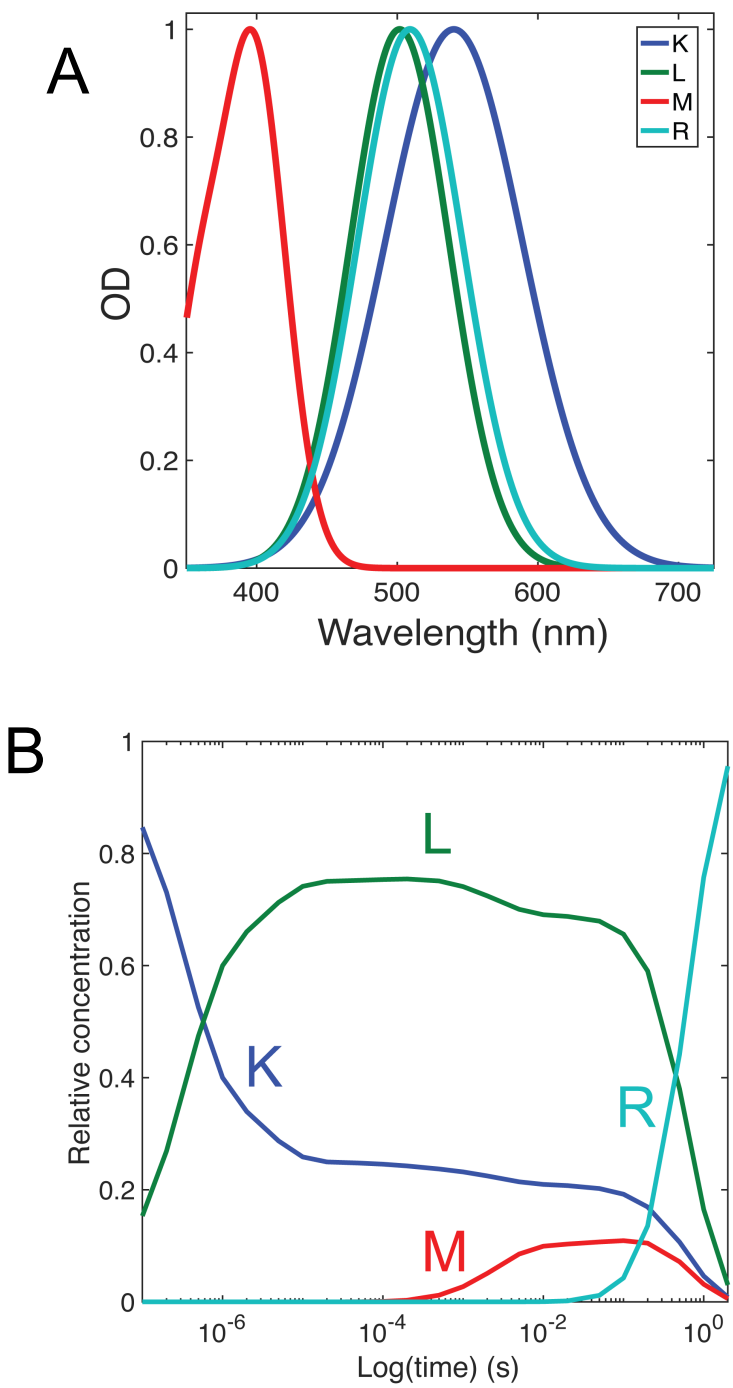

Figure 4.3.25: (A) Absolute intermediate spectra of the A75E mutant determined from decomposing the sequential intermediates into distinct spectra with similar shapes on the energy (wavenumber) scale. **(B)** Time dependent concentration profiles of the absolute intermediate spectra for the A75E mutant.

4.4 Summary

This chapter focused on the investigation of the time-resolved optical absorption of three GtACR1 variants, S97E, D234N, and A75E. Global exponential fitting of the variants revealed similar spectral transitions as those observed for the WT, including two fast components with lifetime ~0.5 μs and ~5 μs, two slow components, ~20-50 ms and ~500 ms, and one or two additional components, the lifetimes of which varied between 100μs-10ms. In all variants, the K and L forms appear to exist for the duration of the experiment. However, much less of the K spectral form appears compared to the WT. These variants are also known to produce less photocurrent.[1,4,7] Unlike the WT, the M form in the D234N mutant appears early in the experiment and is present for a significantly longer time, while for the S97E mutant, hardly any M is present and it forms at the end of the experiment. The S97E revealed a spectrally distinct photointermediate that was indistinguishable to that present in the WT. An in-depth discussion of the results is presented in Chapter 5.

4.5 References

1. Kim, Y. S. *et al.* Crystal structure of the natural anion-conducting channelrhodopsin GtACR1. *Nature* **561**, 343–348 (2018).
2. Li, H. *et al.* Crystal structure of a natural light-gated anion channelrhodopsin. *Elife* **8**, 1–21 (2019).
3. Hasegawa, N., Jonotsuka, H., Miki, K. & Takeda, K. X-ray structure analysis of bacteriorhodopsin at 1.3 Å resolution. *Sci. Rep.* **8**, 13123 (2018).
4. Sineshchekov, O. A., Li, H., Govorunova, E. G. & Spudich, J. L. Photochemical reaction cycle transitions during anion channelrhodopsin gating. *Proc. Natl. Acad. Sci.* **113**, E1993–E2000 (2016).
5. Yi, A., Mamaeva, N., Li, H., Spudich, J. L. & Rothschild, K. J. Resonance raman study of an anion channelrhodopsin: effects of mutations near the retinylidene Schiff base. *Biochemistry* **55**, 2371–2380 (2016).
6. Tsujimura, M., Kojima, K., Kawanishi, S., Sudo, Y. & Ishikita, H. Proton transfer pathway in anion channelrhodopsin-1. *Elife* **10**, 1–17 (2021).
7. Sineshchekov, O. A., Govorunova, E. G., Li, H., Wang, X. & Spudich, J. L. Opposite charge movements within the photoactive site modulate two-step channel closing in GtACR1. *Biophys. J.* **117**, 2034–2040 (2019).

CHAPTER 5

A Discussion on the Photomechanism of GtACR1 and the Identity of the Open-Channel Intermediate

5.1 Evidence in opposition of an unbranched single-chain mechanism

Previous studies on the photomechanism of GtACR1 proposed photocycles that consisted of single chains with no branched steps or side equilibria.[1,2] The first mechanism proposed reversible steps between K and L, followed by a reversible step between L and M, and an irreversible step between M and the late forming intermediates.[1] More recently, a mechanism was proposed with an additional transition that split the L into two forms L1 and L2.[2] The mechanism proposed in this latter study included a reversible step between K and L1, an irreversible step between L1 and L2, a reversible step between L2 and M, and an irreversible step between M and the late intermediates.[2] Below are fragments of the previously proposed mechanisms:

$$K \rightleftharpoons L \rightleftharpoons M \rightarrow R$$

Scheme 5.1: Fragment of a proposed mechanism from ref. 1. Here R is defined as the last intermediate.

$$K \rightleftharpoons L_1 \longrightarrow L_2 \rightleftharpoons M \rightarrow R$$

Scheme 5.2: Fragment of the proposed mechanism from ref. 2. Here R is defined as the last intermediate

In **Chapters 3 and 4** the decomposition of the sequential intermediates revealed a mixture of intermediate spectral forms. In particular, it was shown that each of the sequential intermediates contained some amount of red-absorbing K-like spectral form. The existence of a K form throughout the experiment contradicts the previously proposed mechanisms because the presence of an irreversible step would indicate the absence of K at that step.

The existence of the red-absorbing K form throughout the experiment demonstrates that a single chain of irreversible steps is not adequate to describe the reaction. The results indicate reversible steps between K and other states. Consider the case of a straight sequence of equilibria between K and each spectral form observed at a different apparent lifetime.

$$\mathbf{K} \overset{K_1}{\rightleftharpoons} \mathbf{L1} \overset{K_2}{\rightleftharpoons} \mathbf{L2} \overset{K_3}{\rightleftharpoons} \boldsymbol{L3} \overset{K_4}{\rightleftharpoons} \mathbf{L4} \overset{K_5}{\rightleftharpoons} \mathbf{M} \overset{K_6}{\rightarrow} \mathbf{R}$$

Scheme 5.3: Consecutive 6-step reaction scheme with all steps being reversible

At equilibrium, under the Law of Mass Action, the ratio of products and reactants equals the equilibrium constant.

$$K_1 = \frac{[\boldsymbol{L}]_1}{[\boldsymbol{K}]} \implies [\boldsymbol{L}]_1 = K_1[\boldsymbol{K}]$$

Similarly,

$$[\boldsymbol{L}]_2 = K_2K_1[\boldsymbol{K}] \quad [\boldsymbol{L}]_3 = K_3K_2K_1[\boldsymbol{K}] \quad [\boldsymbol{L}]_4 = K_4K_3K_2K_1[\boldsymbol{K}]$$

Consider the ratio of K to all L forms.

$$\frac{[\boldsymbol{K}]}{\sum_i [\boldsymbol{L}]_i} = \frac{1}{K_1 + K_2K_1 + K_3K_2K_1 + K_4K_3K_2K_1}$$

$$\frac{[\boldsymbol{K}]}{\sum_i [\boldsymbol{L}]_i} = const.$$

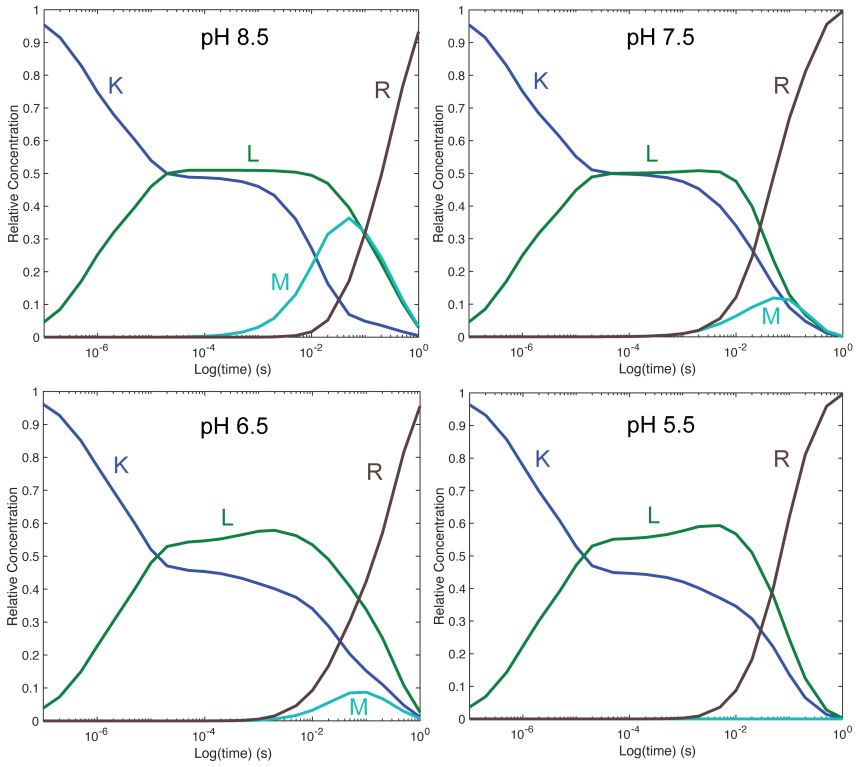

Figure 5.1.1: Time dependent concentration profiles of the absolute intermediate spectra for WT GtACR1 at pH 8.5, 7.5, 6.5, and 5.5.

In other words, for **Scheme 5.3** to be valid, a constant ratio between the amount of K and all L forms should exist before the formation of the M state. However, it is clear from the time dependence of the relative concentration of the spectral forms that the ratio of the K form to the sum of the L forms is not constant over the course of the reaction. Therefore, the reaction mechanism of GtACR1 cannot be solved with a simple replacement of reversible steps in a non-branching single chain scheme.

More complicated mechanisms, including branching steps or side-equilibria, can be difficult to determine as kinetic matrices of these schemes have degenerate solutions. The shapes of the ***b***-spectra can provide clues about the possibility of branching steps in the mechanism.

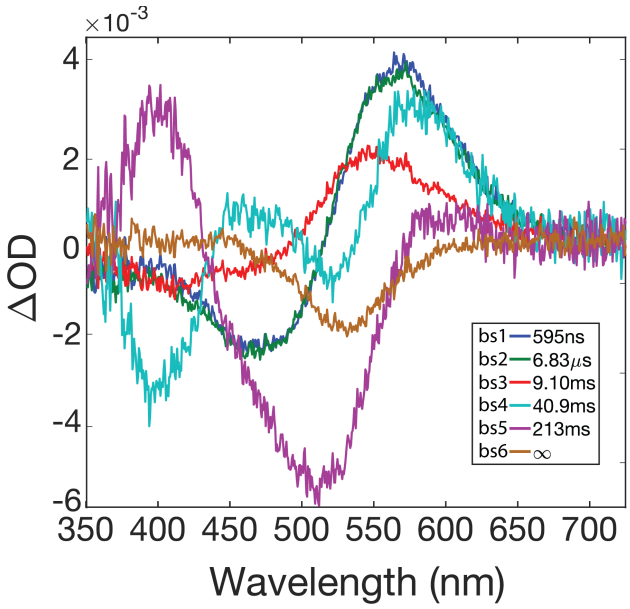

Figure 5.1.2: Spectra of the transitions occurring at each apparent lifetime, also referred to as ***b***-spectra, produced from the 5-exponential fit of the WT GtACR1

The ***b***-spectra are the spectral transitions associated with each apparent lifetime. The shapes of the ***b***-spectra are such that the negative features represent the formation of spectral forms and positive features represent their decay. The ***b***-spectra resulting from the 5-exponential fit of WT GtACR1 at pH 7.5 are shown in **Figure 5.1.2**. A branched step would appear in the ***b***-spectra as a single positive feature with two negative features. Since there is no ***b***-spectrum with this shape, a branching step seems unlikely. However, evidence of isospectral intermediates within the difference spectra was shown in **Chapters 3 and 4**. Isospectral intermediates imply that a branching step cannot be ruled out as an observed spectral feature may contain more than one molecular form causing one intermediate to decay into two. At this point, all that can be concluded is that the mechanism cannot be explained with a single unbranched chain as previously proposed.

5.2 Evidence of the deprotonated Schiff base forming from a red-absorbing species

Previous studies on the photomechanism of WT GtACR1 describe L forms decaying into M.[1,2] The concentration time dependence at pH 8.5 shows a decay of K at the same time as the formation of M, and the concentration of L appears to remain the same while the K form is decreasing. Moreover, the concentration of K appears to increase with decreasing pH where there is less of the deprotonated M form. All of these observations indicate that M is forming from the decay of K rather than L. However, the concentration curve of the D234N and A75E mutants also show a decrease in L at the same time as an increase in M. Thus, it is likely that both the K form and L forms are decaying into M.

5.3 Revelations from mutant kinetics

Important information about the photochemical reaction mechanism was uncovered from analyzing the time-resolved absorption difference spectra of GtACR1 mutants. The absolute spectra of the molecular states determined from decomposing the sequential intermediates of the S97E mutant, along with the time evolution, are presented in **Figure 5.3.1**. The S97E mutant revealed a new molecular intermediate that had been unresolved in the WT. There is always a possibility that similar spectral changes with somewhat different rates are not resolved individually but rather as a single spectral change with an average lifetime. This new intermediate is isospectral, or has the same spectral shape, as the recovered form. We identify this intermediate

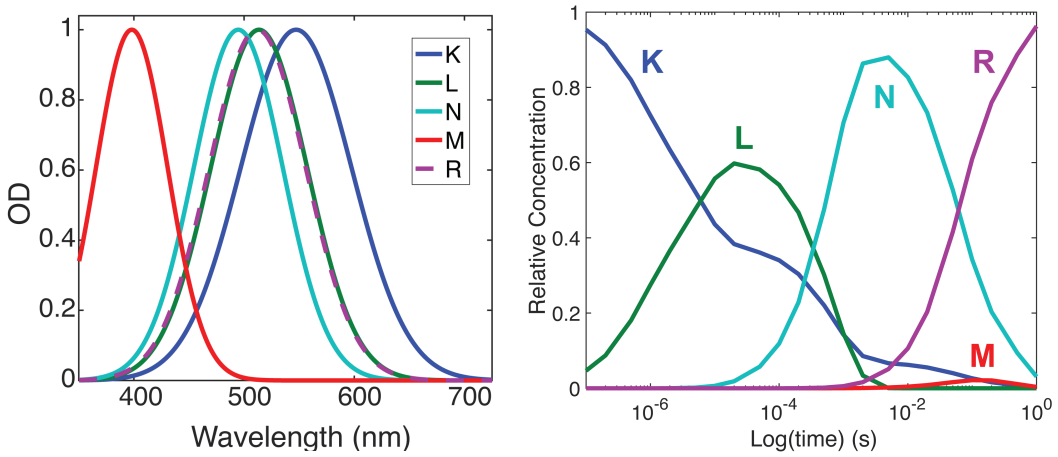

Figure 5.3.1: (A) Absolute intermediate spectral forms determined from decomposing the sequential intermediates of S97E **(B)** Time dependent concentration profiles of the spectral forms for the S97E mutant.

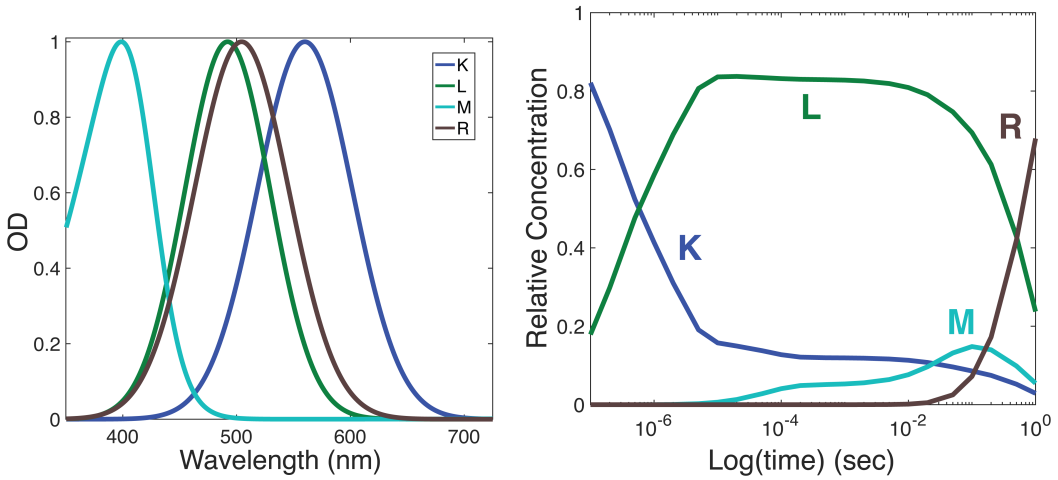

Figure 5.3.2: (A) Absolute intermediate spectral forms determined from decomposing the sequential intermediates of the D234N mutant into distinct spectra with similar shapes on the energy (wavenumber) scale. **(B)** Time dependent concentration profiles of the absolute intermediate spectral forms for the D234N mutant.

spectral form, N, because it appears temporally after L and is spectrally distinct from the deprotonated M form. Furthermore, no M was observed in the S97E mutant.

The time evolution of the S97E absolute spectra suggests an early equilibrium between K and L, similar to that of the WT. It also appears that K and L are decaying at the same time that N is forming, suggesting a mixture of K and L are converting into N. This is confirmed in the ***b***-spectra for the S97E mutant where in the hundreds of microseconds to tens of milliseconds time region a mixture of K, L, and N is observed (see results in **Chapter 4**). The recovered, R, form seems to be formed from the decay of K and N, although a small portion of L may also be converting into the R form. The results from the S97E mutant underscore the existence of isospectral intermediates in the photomechanism of GtACR1 and establishes an alternative reaction pathway that goes through the N state.

Figure 5.3.2 shows the absolute spectra and time evolution of the D234N mutant. Similar to the WT, the decomposition of the D234N intermediate difference spectra produced four unique absolute intermediate spectra, K, L, M, and R. Again, an early equilibrium is established between K and L as can be seen in the tens of microseconds region of the time evolution of the absolute spectra. The M form appears much earlier than in the WT and has a two-component rise with the later rise coinciding with a decay of the K form. This validates the assertation that the K form converts into the deprotonated M state. The ratio of K to L is much lower in the D234N mutant than in the WT or S97E mutant. Some studies on the D234N mutant have reported loss-of-function for this variant.[3,4] A non-conducting variant of GtACR1 would disclose itself

in the photoreaction as an insignificant or absent photointermediate. This suggests that L is unlikely to be the conducting intermediate state as L is a major component for this mutant.

The absolute intermediate spectral forms of the A75E mutant and the time evolution of the spectra are shown in **Figure 5.3.3**. Four unique absolute intermediate spectra were exposed in the analysis, K, L, M, and R. The transitions between different states were well matched temporally to the WT at pH 6.5, which may be explained by the additional acidic functional group within the channel. Laser flash-induced photocurrents of the A75E mutant were reported to be similar to the WT.[5] The ratio of K to L in the A75E mutant was much higher than for the D234N where loss-of-function was reported. This validates the hypothesis that the L forms are not the major component of the conducting state of GtACR1

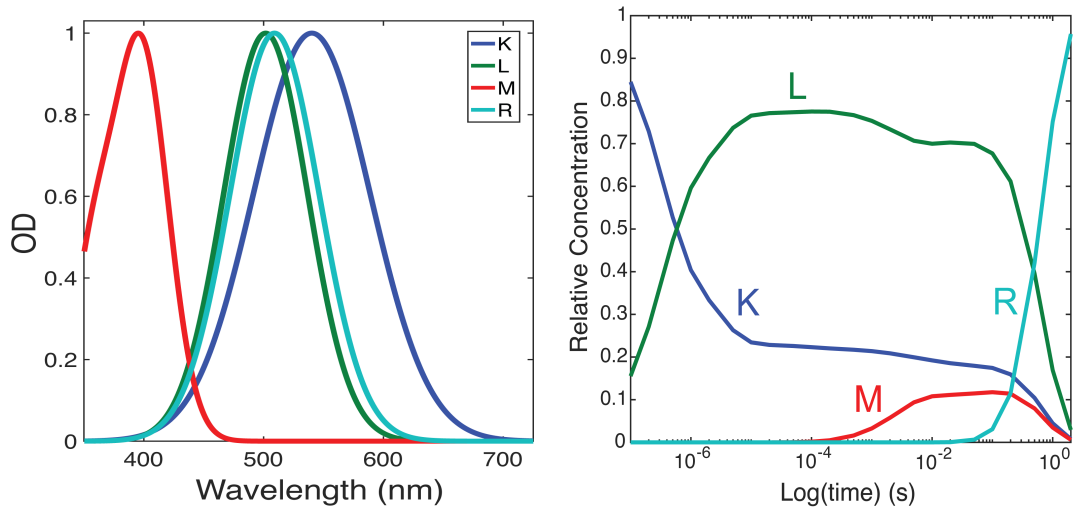

Figure 5.3.3: (A) Absolute intermediate spectral forms of the A75E mutant. **(B)** Time dependent concentration profiles of the spectral forms

5.4 Conclusions

A full mechanistic picture of GtACR1 is still not at hand. The evidence presented here suggests a more complicated mechanism than previously published. There are red-absorbing and blue-absorbing spectral forms that exist for the duration of the experiment and an unbranched single chain mechanism cannot explain these phenomena. Interestingly, the S97E mutant resolved an additional isospectral blue-absorbing intermediate, N. All of the variants in this study had significantly less K relative to L. These variants also have significantly lower photocurrents relative to the WT. The evidence presented here suggests that a red-absorbing K-like species is contributing to the open channel state of the protein as opposed to only a blue-absorbing L-like form.

5.5 Future directions

We cannot say with certainty if N is the same as L2 described by Dreier et al., nor can we concretely define a K form, rather than an L form, as the open channel conformation. To answer both of these questions, structures of the intermediates are sorely needed. GtACR1 is an ideal system for time-resolved serial femtosecond X-ray crystallography experiments. The structure of the dark form of GtACR1 has been solved independently by two separate groups, so a protocol has been established for crystallization in the lipidic cubic phase.[3,6] Moreover, the protein is expected to maintain functional activity in the crystalline state, as many other microbial rhodopsins have been shown to be functionally active when crystallized in the lipidic cubic phase.[7,8] Alternatively, performing time-resolved infrared spectroscopy on the S97E mutant may uncover an additional intermediate that corresponds temporally to the N form we characterized with our TROD measurements. Experiments probing structure would complement the results from this work and advance our understanding on a more complete picture of the photomechanism of GtACR1.

5.6 References

1. Sineshchekov, O. A., Li, H., Govorunova, E. G. & Spudich, J. L. Photochemical reaction cycle transitions during anion channelrhodopsin gating. *Proc. Natl. Acad. Sci.* **113**, E1993–E2000 (2016).
2. Dreier, M. A. *et al.* Time-resolved spectroscopic and electrophysiological data reveal insights in the gating mechanism of anion channelrhodopsin. *Commun. Biol.* **4**, (2021).
3. Kim, Y. S. *et al.* Crystal structure of the natural anion-conducting channelrhodopsin GtACR1. *Nature* **561**, 343–348 (2018).
4. Tsujimura, M., Kojima, K., Kawanishi, S., Sudo, Y. & Ishikita, H. Proton transfer pathway in anion channelrhodopsin-1. *Elife* **10**, 1–17 (2021).
5. Sineshchekov, O. A., Govorunova, E. G., Li, H., Wang, X. & Spudich, J. L. Opposite charge movements within the photoactive site modulate two-step channel closing in GtACR1. *Biophys. J.* **117**, 2034–2040 (2019).
6. Li, H. *et al.* Crystal structure of a natural light-gated anion channelrhodopsin. *Elife* **8**, 1–21 (2019).
7. Mous, S. *et al.* Dynamics and mechanism of a light-driven chloride pump. *Science.* **375**, 845–851 (2022).
8. Skopintsev, P. *et al.* Femtosecond-to-millisecond structural changes in a light-driven sodium pump. *Nature* **583**, 314–318 (2020).